Drag and lift forces on a rigid sphere immersed in a wall-bounded linear shear flow

Pengyu Shi [1,2] Roland Rzehak,[1] Dirk Lucas [1] and Jacques Magnaudet [3,*]
[1]*Helmholtz-Zentrum Dresden–Rossendorf, Institute of Fluid Dynamics, Bautzner Landstrasse 400, D-01328 Dresden, Germany*
[2]*Technische Universität Dresden, Faculty of Mechanical Engineering, Institute of Power Engineering, D-01062 Dresden, Germany*
[3]*Institut de Mécanique des Fluides de Toulouse (IMFT), Université de Toulouse, CNRS, 31400 Toulouse, France*

(Received 16 August 2021; accepted 13 October 2021; published 28 October 2021)

We report on a series of fully resolved simulations of the flow around a rigid sphere translating steadily near a wall, either in a fluid at rest or in the presence of a uniform shear. Nonrotating and freely rotating spheres subject to a torque-free condition are both considered to evaluate the importance of spin-induced effects. The separation distance between the sphere and wall is varied from values at which the wall influence is weak down to gaps of half the sphere radius. The Reynolds number based on the sphere diameter and relative velocity with respect to the ambient fluid spans the range 0.1–250, and the relative shear rate defined as the ratio of the shear-induced velocity variation across the sphere to the relative velocity is varied from -0.5 to $+0.5$, so that the sphere either leads the fluid or lags behind it. The wall-induced interaction mechanisms at play in the various flow regimes are analyzed qualitatively by examining the flow structure, especially the spanwise and streamwise vorticity distributions. Variations of the drag and lift forces at low-but-finite and moderate Reynolds number are compared with available analytical and semiempirical expressions, respectively. In more inertial regimes, empirical expressions for the two force components are derived based on the numerical data, yielding accurate fits valid over a wide range of Reynolds number and wall-sphere separations for both nonrotating and torque-free spheres.

DOI: 10.1103/PhysRevFluids.6.104309

I. INTRODUCTION

Determining the forces acting on particles moving parallel to a wall in a shear flow is of primary importance to understand and predict many features of wall-bounded particle-laden flows. In particular, the wall-normal force component governs crucial phenomena characterizing the dynamics and transfer properties in these flows, such as particle deposition, resuspension, saltation, and near-wall preferential concentration. This force, albeit usually small in magnitude, plays a central role in separation techniques involving nearly neutrally buoyant particles, such as field-flow fractionation or crossflow filtration. Considering very dilute suspensions in which interparticle or wall-particle collisions and direct hydrodynamic interactions play little role, quantitative predictions of how the particles move within the fluid and how in turn their presence possibly affects the flow require accurate expressions for the forces acting on an isolated particle to be available. The present work aims at contributing to this goal by considering a variety of near-wall configurations and flow regimes, identifying the dominant physical mechanisms at play in each of them, and providing

*Corresponding author: jmagnaud@imft.fr

accurate fits for the drag and lift components of the force acting on a spherical particle translating with respect to the wall and obeying either a nonrotating or a torque-free condition.

Due to its symmetrical shape and to the reversibility of Stokes equations, a sphere does not experience any lift force in the creeping-flow regime [1]. Therefore, this force arises through inertial effects associated with the ambient shear and/or the sphere translation and/or rotation with respect to the ambient flow. In a fluid with kinematic viscosity ν, inertial effects associated with these three contributions become comparable to viscous effects at a distance r from the sphere center such that

$$r \sim O(\widetilde{L}_u), \quad r \sim O(\widetilde{L}_\omega), \quad r \sim O(\widetilde{L}_\Omega), \tag{1}$$

respectively. In (1), $\widetilde{L}_u = \nu/|U_{\rm rel}|$, $\widetilde{L}_\omega = (\nu/\gamma)^{1/2}$, and $\widetilde{L}_\Omega = (\nu/\Omega)^{1/2}$ are the so-called Oseen, Saffman, and Magnus lengths, respectively, $U_{\rm rel}$, γ and Ω denoting the relative (or slip) velocity between the sphere and fluid, the shear rate in the undisturbed flow, and the norm of the sphere rotation rate $\mathbf{\Omega}$, respectively. The slip, shear and rotation Reynolds numbers based on the particle diameter d may then be defined as $d/\widetilde{L}_u = |U_{\rm rel}|d/\nu$, $(d/\widetilde{L}_\omega)^2 = \gamma d^2/\nu$, and $(d/\widetilde{L}_\Omega)^2 = \Omega d^2/\nu$, respectively. In an unbounded shear flow, the vorticity generated at the sphere surface is advected asymmetrically in the wake by the ambient shear, yielding a transverse pressure gradient at distances of $O(\widetilde{L}_\omega)$ downstream from the sphere, which results in a lift force directed toward the high- (low-) velocity side if the sphere lags behind (leads) the fluid. A similar mechanism is involved at distances of $O(\widetilde{L}_\Omega)$ in the wake of a spinning sphere translating in a fluid at rest, and results in a Magnus or spin-induced lift force. A closed-form expression was obtained for this force in [2], assuming the slip and rotation Reynolds numbers to be small. If the sphere obeys a torque-free condition, as freely moving particles usually do if they do not collide with another particle or a wall, the spinning rate remains slow, implying $\widetilde{L}_\Omega > \max(\widetilde{L}_u, \widetilde{L}_\omega)$. In this case, the parameter $\varepsilon = \widetilde{L}_u/\widetilde{L}_\omega$ determines whether inertial effects are rather dominated by the ambient shear ($\varepsilon > 1$) or the particle slip ($\varepsilon < 1$). Saffman [3,4] considered a small sphere translating in an unbounded linear shear flow and obtained the shear-induced lift force in closed form in the limit $\varepsilon \gg 1$, assuming the slip and shear Reynolds numbers to be small. His prediction was extended to finite ε in [5] and [6], the results revealing that the lift force strongly decreases as the relative influence of the sphere translation increases, i.e., as ε decreases. Experiments [7] and simulations [8] have confirmed these predictions down to $\varepsilon \approx 0.4$ for particles with slip Reynolds numbers up to unity. Further insight into the shear-induced lift force in an unbounded fluid at higher Reynolds number was obtained through numerical studies [9,10], revealing in particular that the distribution of the viscous stresses in the recirculating flow region at the back of the sphere makes this force reverse beyond a slip Reynolds number of some tens. Influence of the sphere rotation on the drag and lift forces in inertia-dominated regimes has also been examined, both for an imposed spinning motion and a torque-free condition [9,11].

When the flow is bounded by a single flat wall, the separation distance $\widetilde{L}$ from the sphere center to the wall competes with the above three visco-inertial length scales through the ratios

$$L_u = \widetilde{L}/\widetilde{L}_u = \frac{\widetilde{L}|U_{\rm rel}|}{\nu}, \quad L_\omega = \widetilde{L}/\widetilde{L}_\omega = \frac{\widetilde{L}\gamma^{1/2}}{\nu^{1/2}}, \quad L_\Omega = \widetilde{L}/\widetilde{L}_\Omega = \frac{\widetilde{L}\Omega^{1/2}}{\nu^{1/2}}, \tag{2}$$

which may be thought of as Reynolds numbers based on $\widetilde{L}$ rather than on the particle size. In the sense of matched asymptotic expansions, the wall is located in the inner region of the disturbance if $\max(L_u, L_\omega, L_\Omega) < 1$ (strictly speaking $\ll 1$), while it stands in the outer region otherwise. Fundamental results were established by Cox and Brenner [12] in the former case, showing in particular that, owing to the screening effect exerted by the wall, the leading-order estimate of the lift force may then be obtained through a regular expansion procedure. This work also enlightened the manner in which the generalized reciprocal theorem may be employed to obtain the lift force in the form of a volume integral solely involving creeping-flow solutions past the sphere.

Asymptotic predictions for the slip-induced lift force acting on rigid spheres sedimenting close to a vertical wall in a fluid at rest in the low-Reynolds-number regime were obtained in [13] (based on the results of [12]) and [14], assuming that the wall lies in the inner and outer regions of

the disturbance, respectively. In this configuration, the lift force always tend to repel the particle from the wall and decreases gradually with increasing L_u. Considering the physical origin of the wall-particle interaction responsible for this force, which directly stems from wall-induced corrections to the flow in the wake region, the prediction of [14] was extended in a semiempirical manner up to slip Reynolds numbers of $O(100)$, based on experiments performed with contaminated nearly spherical air bubbles [15]. Fully resolved simulations [16,17] subsequently confirmed this semiempirical prediction.

Still in the low-but-finite Reynolds number regime, predictions for the shear-induced lift force in the presence of a wall standing in the inner region of the disturbance were also obtained in [13], for both neutrally buoyant and negatively or positively buoyant particles. These results were then extended to the case of a wall standing in the outer region, first in the limit $\varepsilon \gg 1$ [18], and then for arbitrary ε [5,19]. These predictions were found to be valid up to slip Reynolds numbers of order unity in experiments performed under conditions $\varepsilon \lesssim 1$ [20,21]. They bridge the gap between those of [13] and [6] (hence [3] in the limit $\varepsilon \gg 1$), the latter being recovered in the limit where the wall is moved to infinity. While the slip-induced and shear-induced contributions to the lift superimpose linearly when the wall stands in the inner region, they are intrinsically coupled otherwise, owing to the nonlinear nature of the Oseen equation. Both contributions are directed away from the wall if the sphere lags behind the fluid, which is the case for a negatively (positively) buoyant particle in an upward (downward) shear flow near a vertical wall. Conversely, if the sphere leads the fluid, as for a light (heavy) particle in an upward (downward) shear flow, the shear-induced contribution tends to attract it toward the wall. In this case, the total lift force is attractive for large enough separations, but becomes repulsive again for short separations. This is because the wall influence gradually weakens the shear-induced contribution as the separation decreases, making the slip effect eventually dominant very close to the wall. In the above studies, the wall was considered sufficiently distant from the particle for the latter to be shrunk to a point. Obviously, this approximation is not tenable when the separation becomes of the order of a few sphere radii or less. Higher-order corrections accounting for the sphere finite size were obtained through the "reflection" technique [22] (see also Appendix A of [23]), but this approach cannot deal with situations in with the gap is less than typically the sphere radius. The combined use of exact creeping-flow solutions based on bispherical coordinates and the generalized reciprocal theorem allowed rational fits for the various contributions to the lift force to be obtained down to very small separations for both nonrotating and torque-free spheres [23–25]. The limit case of a sphere held fixed on the wall, and that of a freely sliding and rolling sphere were worked out in [26] and [27], respectively.

Numerical studies of hydrodynamic forces in near-wall configurations are quite scarce, presumably because they demand accurate boundary-fitted grids or refined immersed boundary techniques to properly capture the flow within the wall-particle gap. Variations of the slip- and shear-induced drag and lift forces in the low-but-finite Reynolds number regime with the wall located in either region of the disturbance were recently explored for both neutrally buoyant particles [28] and arbitrarily buoyant particles [29]. The characteristics of the slip-induced lift force in a wall-bounded fluid at rest were examined in detail in [16] and [17] down to small gaps and from Reynolds numbers of $O(1)$ up to a few hundred. The same range of separations and Reynolds numbers was considered in [17] for a sphere held fixed with respect to the wall in a linear shear flow, a very specific choice corresponding to $L_u = L_\omega^2$. Near-wall forces acting on a sphere forced to spin in a fluid at rest were determined in [30] over a quite similar range of parameters, together with those experienced by a sphere immersed in a shear flow which either slides on the wall or spins very close to it.

From the above review it appears that no study has considered inertia-dominated regimes for an arbitrarily translating and possibly freely rotating rigid sphere immersed in a wall-bounded shear flow, a situation of particular relevance to the widely encountered case of buoyant particles moving near a vertical wall. This is the problem addressed in the present work. The same problem was recently considered in [31] for spherical bubbles with a clean, i.e., shear-free, surface. Compared to the rigid sphere case, this difference in the dynamic boundary condition at the particle surface is known to affect the magnitude of the wall-induced forces in the low-Reynolds-number regime, but

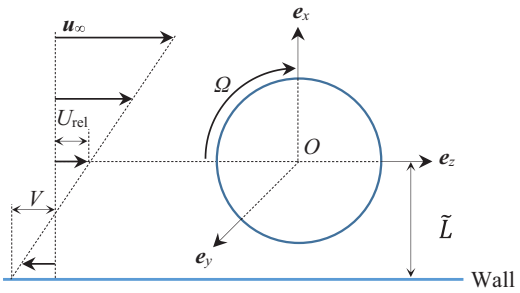

FIG. 1. Schematic of a sphere moving in a wall-bounded linear shear flow.

not the manner they vary with the flow parameters [22]. This is no longer the case beyond Reynolds numbers of a few units, due to the much larger amount of vorticity produced at the sphere surface when the no-slip condition applies. In particular this difference results in the fact that the flow does not separate past a spherical bubble even at large Reynolds number while it does past a rigid sphere beyond a Reynolds number of $O(10)$.

In what follows we report on the results of fully resolved simulations of the flow past a freely translating and possibly rotating sphere. The sphere is immersed in a wall-bounded linear shear flow, may either lead the fluid or lag behind it, and obeys a nonrotating or a torque-free condition. In Sec. II we formulate the problem, specify the considered range of parameters and outline the numerical approach which is essentially similar to that employed in [31]. Section III summarizes theoretical and semiempirical expressions for the forces acting on a sphere in an unbounded shear flow and in wall-bounded configurations. Numerical results are first used in Sec. IV to examine the physical mechanisms induced by the presence of the wall and the corresponding alterations of the near-sphere flow in the various regimes. Variations of the drag and lift forces with the flow parameters are analyzed in Sec. V. Empirical fits reproducing the observed variations in specific regimes or throughout the entire parameter range of the simulations are established. A summary of the main outcomes, especially regarding these empirical fits of direct interest in applications, is provided in Sec. VI.

II. STATEMENT OF THE PROBLEM AND OUTLINE OF THE SIMULATION APPROACH

We define a Cartesian coordinate system $(Oxyz)$ with the origin located at the center of the sphere, as illustrated in Fig. 1. We assume that the sphere moves parallel to a single planar wall with a translational velocity $\boldsymbol{V} = V\boldsymbol{e}_z$ and a rotational velocity $\boldsymbol{\Omega} = -\Omega\boldsymbol{e}_y$. The wall is located at $x = -\widetilde{L}$ and $\boldsymbol{e}_x$ denotes the wall-normal unit vector pointing into the fluid. In the reference frame translating with the sphere, the undisturbed flow is a one-dimensional linear shear flow with a velocity profile $\boldsymbol{u}_\infty = [\gamma(\widetilde{L} + x) - V]\boldsymbol{e}_z$ and a spanwise vorticity $\boldsymbol{\omega}_\infty = -\gamma\boldsymbol{e}_y$. The relative (or slip) velocity of the fluid with respect to the sphere is then $\boldsymbol{U}_{\rm rel} = (\gamma\widetilde{L} - V)\boldsymbol{e}_z$. The fluid velocity and pressure fields in the presence of the sphere are denoted by $\boldsymbol{u}$ and p, respectively, and $\boldsymbol{\omega} = \boldsymbol{\nabla} \times \boldsymbol{u}$ denotes the vorticity.

Assuming the fluid to be Newtonian and considering the flow as incompressible, the continuity and Navier-Stokes equations read

$$\boldsymbol{\nabla} \cdot \boldsymbol{u} = 0\,; \quad \frac{\partial \boldsymbol{u}}{\partial t} + \boldsymbol{u} \cdot \boldsymbol{\nabla}\boldsymbol{u} = -\frac{1}{\rho}\boldsymbol{\nabla} p + \nu\nabla^2\boldsymbol{u}, \tag{3a,b}$$

with ρ and ν the fluid density and kinematic viscosity, respectively. Boundary conditions at the sphere surface, at the wall, and in the far field read, respectively,

$$\boldsymbol{u} = \begin{cases} \boldsymbol{\Omega} \times \boldsymbol{r} & \text{for} \quad r = d/2, \\ -V\boldsymbol{e}_z & \text{for} \quad x = -\widetilde{L}, \\ \boldsymbol{u}_\infty = [\gamma(\widetilde{L} + x) - V]\boldsymbol{e}_z & \text{for} \quad r \to \infty, \end{cases} \tag{4}$$

where $r = (x^2 + y^2 + z^2)^{1/2}$ denotes the distance to the sphere center, and d is the sphere diameter.

With the above boundary conditions, the steady flow field past the sphere depends on four characteristic parameters, namely, the slip Reynolds number, Re, the dimensionless shear rate, Sr, the dimensionless sphere rotation rate, Rr, and the normalized wall distance, L_R. These control parameters are defined as

$$\mathrm{Re} = \frac{|U_\mathrm{rel}|d}{\nu}, \quad \mathrm{Sr} = \frac{\gamma d}{U_\mathrm{rel}}, \quad \mathrm{Rr} = \frac{\Omega d}{U_\mathrm{rel}}, \quad L_\mathrm{R} = \frac{2\widetilde{L}}{d}, \tag{5}$$

with $U_\mathrm{rel} = \boldsymbol{U}_\mathrm{rel} \cdot \boldsymbol{e}_z$ and $\Omega = -\boldsymbol{\Omega} \cdot \boldsymbol{e}_y$. Under the torque-free condition, Rr is entirely determined by the other three parameters and is no longer an independent control parameter. Considering that the slip velocity U_rel may either be positive or negative while γ and Ω are always positive, Sr and Rr change sign with U_rel. A positive (negative) Sr indicates that the sphere lags (leads) the fluid, the former case corresponding to the flow configuration sketched in Fig. 1. In most of this work, Re, Sr, and L_R are varied in the range [0.1, 250], [−0.5, 0.5], and [1.5, 8], respectively. Hence ε is up to 2.2 for $\mathrm{Re} = 0.1$ and becomes less than 1 as soon as $\mathrm{Re} > 0.5$, and even less than 0.1 beyond $\mathrm{Re} = 50$. In an unbounded fluid, the shear-induced transverse force is proportional to Sr, so that its sign changes with that of U_rel. In the presence of a nearby wall, three different regimes are encountered. If $\mathrm{Sr} \ll 1$, the transverse force results primarily from the particle relative translation with respect to the wall, which at low-but-finite Reynolds number makes it proportional to Re. In contrast, when $\mathrm{Sr} \gg 1$, i.e., the slip velocity is small compared to the shear-induced velocity variation at the particle scale, the dominant contribution to the transverse force is proportional to Sr^2. This regime, relevant to small nearly neutrally buoyant particles, will not be considered here (it was recently specifically examined in [28,32] in the low-Re range, with applications to inertial microfluidics in mind). The near-wall transverse force does not change sign with U_rel in the above two regimes, being repulsive in both cases. In contrast, it may change sign when $\mathrm{Sr} \lesssim 1$, which is the regime we are primarily interested in.

Let us briefly illustrate some flow configurations covered by the above parameter range. Consider for instance a 1-mm-diameter particle sedimenting in water and assume the particle is twice as dense as the fluid. Then the standard drag law predicts that its slip Reynolds number is approximately 115. With $|\mathrm{Sr}| = 0.5$, this yields $\gamma \approx 57\ \mathrm{s}^{-1}$. This is, for instance, the near-wall shear rate in the laminar flow in a 15-mm-high plane channel, the corresponding Reynolds number $\mathrm{Re_H}$ based on the channel height and depth-averaged fluid velocity being $\mathrm{Re_H} \approx 2200$. In the same configuration, a particle ten times smaller ($d = 0.1\,\mathrm{mm}$) has a slip Reynolds number close to 0.55 and the shear rate corresponding to $|\mathrm{Sr}| = 0.5$ is $27\ \mathrm{s}^{-1}$, the near-wall value reached in a 1.5-mm-high channel with $\mathrm{Re_H} \approx 10$. Consider now that the largest of the above two particles is immersed in a vertical turbulent boundary layer and stands 1 mm apart from the wall (which corresponds to $L_\mathrm{R} = 2$) in the logarithmic region. Then, equating γ to the local time-averaged shear rate $u^*/(\kappa L_\mathrm{R})$, with $\kappa = 0.4$ the von Kármán constant, the associated friction velocity u^* is close to $2.25\ \mathrm{cm\,s}^{-1}$, which corresponds to an outer velocity close to $0.6\ \mathrm{m\,s}^{-1}$, i.e., $\mathrm{Re_H} \approx 3 \times 10^4$ if the flow takes place in a 5-cm-high channel. Still with $L_\mathrm{R} = 2$, the $d = 0.1\,\mathrm{mm}$ particle rather stands within the viscous sublayer. There, the time-averaged shear rate corresponding to $|\mathrm{Sr}| = 0.5$ is $\gamma = u^{*2}/\nu \approx 27\ \mathrm{s}^{-1}$, which yields $u^* \approx 5.2\ \mathrm{mm\,s}^{-1}$, hence an outer velocity close to $15\ \mathrm{cm\,s}^{-1}$ corresponding to $\mathrm{Re_H} \approx 7500$.

In the present problem, the drag force F_D parallel to $\boldsymbol{U}_\mathrm{rel}$, i.e., parallel or antiparallel to $\boldsymbol{e}_z$ depending on whether the sphere lags or leads the fluid, the lift force parallel to $\boldsymbol{e}_x$, F_L, and the

torque antiparallel to $\boldsymbol{e}_y$, M, acting on the sphere are defined as

$$F_{\mathrm{D}} = \frac{\boldsymbol{U}_{\mathrm{rel}}}{||\boldsymbol{U}_{\mathrm{rel}}||} \cdot \int_{\Gamma} \boldsymbol{\Sigma} \cdot \boldsymbol{n}\, d\Gamma, \quad F_{\mathrm{L}} = \boldsymbol{e}_x \cdot \int_{\Gamma} \boldsymbol{\Sigma} \cdot \boldsymbol{n}\, d\Gamma, \quad M = -\boldsymbol{e}_y \cdot \int_{\Gamma} \boldsymbol{r} \times (\boldsymbol{\Sigma} \cdot \boldsymbol{n})\, d\Gamma, \tag{6}$$

where $\boldsymbol{\Sigma}$ is the stress tensor and $\boldsymbol{n}$ denotes the outward unit normal to the sphere surface Γ. Results concerning the two force components will be expressed in terms of the lift and drag coefficients, C_{L} and C_{D}, obtained by dividing the corresponding force by $\pi d^2 \rho U_{\mathrm{rel}}^2/8$. According to the above definition, a negative (positive) C_{L} corresponds to a force directed toward (away from) the wall. In the case of a nonrotating sphere, results concerning the hydrodynamic torque will be expressed using the torque coefficient $C_{\mathrm{M}} = M/(\pi d^3 \rho U_{\mathrm{rel}}^2/16)$. We use the notations $C_{\mathrm{D}}^{\mathrm{W}}$ ($C_{\mathrm{L}}^{\mathrm{W}}$) and $C_{\mathrm{D}}^{\mathrm{U}}$ ($C_{\mathrm{L}}^{\mathrm{U}}$) to denote the drag (lift) coefficients in wall-bounded and unbounded flows, respectively. Situations where the wall lies in the inner or outer region of the disturbance will be distinguished by superscripts W-in and W-out, respectively. Results for the drag coefficient are usually given in the form of the relative wall-induced change $\Delta C_{\mathrm{D}} = (C_{\mathrm{D}}^{\mathrm{W}} - C_{\mathrm{D0}}^{\mathrm{U}})/C_{\mathrm{D0}}^{\mathrm{U}}$, with $C_{\mathrm{D0}}^{\mathrm{U}}$ denoting the drag coefficient on a sphere translating in an unbounded uniform fluid. Drag (lift) contributions corresponding to the slip-induced effect are denoted with the subscript Du (Lu), while those corresponding to the shear-induced effect are denoted with the subscript Dω (Lω). Similar conventions are applied to the rotation rate, Rr.

The three-dimensional flow field past the sphere is computed with the JADIM code developed at IMFT. The sphere center stands on the axis of a large cylindrical computational domain, one base of which coincides with the wall. The reader is referred to [31] for numerical aspects concerning the specificities of the code, the grid system, and the boundary conditions. The only difference between the present problem and that considered in [31] is the boundary condition at the particle surface, the shear-free condition suitable for a clean bubble being now replaced by a no-slip condition. The consequence of this change on the flow field is that stronger velocity gradients, hence larger levels of vorticity, are encountered around a rigid sphere. The increase in the vorticity magnitude is modest at low Reynolds number. In contrast it is large at high Reynolds number, especially within the boundary layer and the near wake, since the vorticity in the former varies like $\mathrm{Re}^{1/2}$ in the presence of a no-slip condition while it becomes Re-independent with a shear-free condition. However, the boundary layer thickness is of $O(d\mathrm{Re}^{-1/2})$ in both cases. The difference in the vorticity magnitude has a dramatic influence on the nature of the flow when the Reynolds number exceeds a few hundred. In particular, in an unbounded domain with the fluid at rest at infinity, the flow past a steadily translating spherical bubble remains stationary and axisymmetric whatever Re. In contrast, the axial symmetry of a rigid sphere wake is known to break down at $\mathrm{Re} \approx 212$, while the flow becomes unsteady beyond $\mathrm{Re} \approx 272$ [33]. In [31] the grid was designed in such a way that the flow was properly described up to $\mathrm{Re} = 10^3$, especially within the wall and bubble boundary layers. Here, since we wish to focus on stationary regimes, we consider only Reynolds numbers up to $\mathrm{Re} = 250$. Similar to [31], the size of the computational domain is varied with Re so as to minimize confinement effects in all flow regimes. Since no vortex shedding is expected downstream of the sphere up to the maximum Reynolds number considered here, we keep the domain size unchanged compared to the bubble case. That is, the radius R_∞ and height of the domain from the sphere center to the top of the cylinder are set to $50d$ for $\mathrm{Re} < 1$, $40d$ for $1 \leqslant \mathrm{Re} < 100$, and $20d$ for $\mathrm{Re} \geqslant 100$, respectively. The grid makes use of 128 uniformly distributed cells along the azimuthal direction (i.e., the cylinder periphery), while 60 cells are employed to describe the sphere surface from pole to pole (only half that number was used in the bubble case). Given the maximum Reynolds number of 250, the thinnest boundary layers expected here are typically twice as thick as those considered in [31]. Nevertheless, the velocity gradients being larger, we keep the same discretization in the direction normal to the sphere surface. That is, with $R_\infty = 20d$, the first node stands a distance $10^{-3}d$ from this surface in the equatorial plane ($x = 0$). The grid being strongly nonuniform in the radial direction, a total of 54 cells is used in that direction irrespective of R_∞, with a typical number of 12 cells standing within the boundary layer at $\mathrm{Re} = 250$. Along the cylinder axis, the discretization is identical to that used in the bubble case. That is, 58 cells are

nonuniformly distributed from the pole opposed to the wall ($x = d/2, y = z = 0$) to the top of the cylinder ($x = R_\infty$), while the number of cells in between the other pole ($x = -d/2, y = z = 0$) and the wall is varied from 10 to 40 depending on L_R and Re in the manner detailed in [31]. Some runs were also performed to obtain reference values in an unbounded shear flow. In these cases, we set $\widetilde{L} = R_\infty$ (with the aforementioned Re-dependent values of R_∞) in order to keep the domain symmetric.

Comparison with available data and asymptotic predictions available for a clean bubble, together with grid convergence tests, were presented in [31]. In the rigid sphere case, extensive comparisons and grid convergence tests in both wall-bounded and unbounded shear flows were reported in [34]. Results obtained with the grid characteristics described above were shown to compare well with those of [16,17] in the former case and those of [35] (once properly transposed to a rigid sphere) and [9,11] in the latter case. As will become apparent in Sec. V, the most convincing comparison in wall-bounded configurations is for the case of a translating particle in a fluid at rest (Figs. 10 and 12), since data from [16] span a parameter range close to that explored here. In wall-bounded shear flows, available studies ([29] in the low-Re range, [17,30] for moderate-to-large Re) only marginally overlap the parameter space considered here. Whenever possible, comparisons with these data will be presented in Sec. V B. In the unbounded shear flow configuration, some comparisons with Refs. [9,11] for the lift force on a nonrotating sphere will also be provided in Figs. 18 and 19, while the rotation rate on a torque-free sphere will be compared with the fit based on the results from [11] in Fig. 21.

To achieve the torque-free condition, the sphere rotation rate Rr is computed through an iterative approach. First, the steady flow around a nonrotating sphere is determined to obtain the corresponding torque coefficient, C_{M0}. Then the rotation rate is updated as $\mathrm{Rr}_1 = \mathrm{Rr}_0 + C_{M0}\mathrm{Re}/16$ and the corresponding steady flow field is determined to obtain the new torque coefficient, C_{M1}. This procedure is continued until the torque coefficient becomes less than $0.05C_{M0}$. In the Appendix we show how this procedure converges in a wall-bounded shear flow at two widely different Reynolds numbers. We also report sensitivity tests proving that the forces acting on the particle, especially the lift force, only marginally vary (typically by 1% for the latter) when the rotation rate is varied from the value achieving a torque coefficient of $0.05C_{M0}$ to the value corresponding to the strict torque-free condition.

III. ANALYTICAL SOLUTIONS AND EMPIRICAL PREDICTIONS

A. Unbounded linear shear flow

At low-but-finite Reynolds number, the presence of a uniform shear in an unbounded flow domain results in a transverse or lift force on a sphere in the direction of $\boldsymbol{U}_{\mathrm{rel}} \times \boldsymbol{\omega}$. For $\mathrm{Sr} \gg 1$, the leading-order force is proportional to $(|\mathrm{Sr}|/\mathrm{Re})^{1/2}$. In the case of a nonrotating sphere, the corresponding lift coefficient takes the form [5,6]

$$C^{\mathrm{U}}_{\mathrm{L}\omega}(\mathrm{Re} \ll 1) = \frac{18}{\pi^2}\mathrm{sgn}(\mathrm{Sr})\varepsilon J_{\mathrm{L}}(\varepsilon), \tag{7}$$

where $\varepsilon = \widetilde{L}_u/\widetilde{L}_\omega = (|\mathrm{Sr}|/\mathrm{Re})^{1/2}$ is the ratio of the Oseen and Saffman lengths, and $\mathrm{sgn}(\mathrm{Sr}) = \mathrm{Sr}/|\mathrm{Sr}|$. Saffman's original result [3] corresponds to the limit $\varepsilon \gg 1$ for which $J_{\mathrm{L}}(\varepsilon) \to 2.254$. In [6] the prefactor $J_{\mathrm{L}}(\varepsilon)$ was obtained for arbitrary ε in the form of a three-dimensional integral which was evaluated numerically for specific values of ε. Based on fully resolved simulations at low Reynolds number and $\mathrm{Sr} \leqslant 0.5$, a useful approximation of $J_{\mathrm{L}}(\varepsilon)$ was established in [35] in the form

$$J_{\mathrm{L}}(\varepsilon) \approx 2.254(1 + 0.2\varepsilon^{-2})^{-3/2}. \tag{8}$$

Assuming Re and ReRr to be small, a rotating sphere translating in a fluid at rest experiences a transverse force $\frac{\pi}{8}\rho d^3 \boldsymbol{\Omega} \times \boldsymbol{U}_{\mathrm{rel}}$ [2], which yields a lift coefficient $C^{\mathrm{U}}_{\mathrm{L}\Omega}[\mathrm{Re} \ll 1] = \mathrm{Rr}$. When ambient shear and rotation act together, the total lift force including $O(\mathrm{Rr})$ and $O(\mathrm{Sr})$ effects is

the sum of the two individual contributions, and involves a second-order shear-induced contribution lowering the lift coefficient by $-\frac{11}{8}\mathrm{Sr}$ in the limit $|\mathrm{Sr}| \gg 1$ [3]. Therefore, the total lift coefficient takes the form

$$C_{\mathrm{L}\omega}^{\mathrm{U}}(\mathrm{Re} \ll 1) \approx \frac{18}{\pi^2}\mathrm{sgn}(\mathrm{Sr})\varepsilon J_{\mathrm{L}}(\varepsilon) - \frac{11}{8}\mathrm{Sr} + \mathrm{Rr}. \tag{9}$$

If the torque-free condition holds, the leading-order sphere rotation rate in the low-Re regime is half the undisturbed flow vorticity:

$$\mathrm{Rr} = \mathrm{Rr}^{\mathrm{U}}(\mathrm{Re} \ll 1) \approx \tfrac{1}{2}\mathrm{Sr}. \tag{10}$$

Consequently, the rotation-induced and second-order shear-induced lift forces combine in a correction of $-\frac{7}{8}\mathrm{Sr}$ to (7) [3].

At low-to-moderate Reynolds numbers, the shear-induced lift force predicted by (7) agrees well with numerical data for nonrotating spheres up $\mathrm{Re} \approx 10$ [9]. Increasing Re, this force first exhibits weak positive values up to $\mathrm{Re} \approx 50$. Beyond this range, it changes sign, owing to the influence of the standing eddy on the stress distribution at the rear of the sphere. For $\mathrm{Re} \gtrsim 50$, the numerical results of [9] and [11] are adequately fitted by the empirical correlation [36]

$$C_{\mathrm{L}\omega}^{\mathrm{U}}[\mathrm{Re} = O(100)] \approx -\mathrm{sgn}(\mathrm{Sr})|\mathrm{Sr}|^{1/3}\left\{0.0525 + 0.0575\tanh\left[11.5\log\left(\frac{\mathrm{Re}}{120}\right)\right]\right\}. \tag{11}$$

The spin-induced lift coefficient $C_{\mathrm{L}\Omega}^{\mathrm{U}}(\mathrm{Re})$ remains linearly proportional to the rotation rate at moderate Reynolds number. Setting $C_{\mathrm{L}\Omega}^{\mathrm{U}}(\mathrm{Re}) = c_{\mathrm{L}\Omega}^{\mathrm{U}}(\mathrm{Re})\mathrm{Rr}$, the coefficient $c_{\mathrm{L}\Omega}^{\mathrm{U}}$ is found to be smaller than unity and nearly independent of the Reynolds number for $\mathrm{Re} \gtrsim 1$. According to [11], one has at moderate Re

$$c_{\mathrm{L}\Omega}^{\mathrm{U}}[\mathrm{Re} = O(1-100)] \approx 0.55. \tag{12}$$

In the same range of Reynolds number, the torque-free spin rate normalized by the ambient rotation rate is found to depend only on Re in the form [11]

$$\mathrm{Rr} = \mathrm{Rr}^{\mathrm{U}}[\mathrm{Re} = O(1-100)] \approx f_{\Omega}^{\mathrm{U}}(\mathrm{Re})\frac{\mathrm{Sr}}{2} \tag{13}$$

with

$$\begin{aligned} f_{\Omega}^{\mathrm{U}}(\mathrm{Re}) &\approx 1 - 0.0364\mathrm{Re}^{0.95} \quad \text{for} \quad 0.5 \leqslant \mathrm{Re} \leqslant 5 \quad \text{and} \\ f_{\Omega}^{\mathrm{U}}(\mathrm{Re}) &\approx 1 - 0.0755\mathrm{Re}^{0.455} \quad \text{for} \quad \mathrm{Re} > 5. \end{aligned} \tag{14}$$

Available DNS results for torque-free rotating spheres suggest that contributions of shear and rotation still superpose linearly in the lift force up to $\mathrm{Re} = 100$ [37].

B. Low-*Re* wall-bounded shear flow

The presence of a nearby wall results in a drag increase, while for reasons mentioned above it may either increase or decrease the transverse force, depending on the sign of Sr. For $\mathrm{Re} \ll 1$, situations where the wall lies in the inner region of the disturbance, i.e., $\max(L_u, L_\omega, L_\Omega) \ll 1$, were investigated in [13,22,23,38,39].

In the case of a nonrotating sphere, the results of [23] indicate that the lift coefficient is approximately [40]

$$C_{\mathrm{L}}^{\text{W-in}}(\mathrm{Sr}, L_{\mathrm{R}}) = \underbrace{\tfrac{9}{8}\left(1+\tfrac{1}{8}L_{\mathrm{R}}^{-1}-0.413L_{\mathrm{R}}^{-2}+0.270L_{\mathrm{R}}^{-3}\right)}_{C_{\mathrm{L}u}^{\text{W-in}}} + \underbrace{\tfrac{33}{32}\left(L_{\mathrm{R}}+\tfrac{17}{48}+0.643L_{\mathrm{R}}^{-1}-0.280L_{\mathrm{R}}^{-2}\right)\mathrm{Sr}+\tfrac{61}{192}\left(1+0.527L_{\mathrm{R}}^{-1}-1.200L_{\mathrm{R}}^{-2}+0.657L_{\mathrm{R}}^{-3}\right)\mathrm{Sr}^2}_{C_{\mathrm{L}\omega}^{\text{W-in}}}. \tag{15}$$

Similarly, in the case of a torque-free rotating sphere, one has

$$C_{\mathrm{L}}^{\text{W-in}}(\mathrm{Sr}, L_{\mathrm{R}}) = \underbrace{\tfrac{9}{8}\left(1+\tfrac{3}{16}L_{\mathrm{R}}^{-1}-0.511L_{\mathrm{R}}^{-2}+0.287L_{\mathrm{R}}^{-3}\right)}_{C_{\mathrm{L}u}^{\text{W-in}}} + \underbrace{\tfrac{33}{32}\left(L_{\mathrm{R}}+\tfrac{443}{528}+0.258L_{\mathrm{R}}^{-1}-0.145L_{\mathrm{R}}^{-2}\right)\mathrm{Sr}+\tfrac{55}{192}\left(1+\tfrac{9}{16}L_{\mathrm{R}}^{-1}-1.090L_{\mathrm{R}}^{-2}+0.568L_{\mathrm{R}}^{-3}\right)\mathrm{Sr}^2}_{C_{\mathrm{L}\omega}^{\text{W-in}}}. \tag{16}$$

The difference between (15) and (16) indicates an increase of the lift coefficient by $\frac{1}{2}\mathrm{Sr}$ and a decrease by $-\frac{1}{32}\mathrm{Sr}^2$ for large L_{R}, when switching from the zero-rotation condition to the zero-torque one. The $\frac{1}{2}\mathrm{Sr}$-increase is in line with the contribution of the torque-free rotation to the lift force found in the unbounded case.

Still for a torque-free sphere, the dimensionless rotation rate is approximately [22,38,39]

$$\mathrm{Rr}^{\text{W-in}}(\mathrm{Sr}, L_{\mathrm{R}}) \approx \underbrace{-\tfrac{3}{16}L_{\mathrm{R}}^{-4}\left(1-\tfrac{3}{8}L_{\mathrm{R}}^{-1}\right)}_{\mathrm{Rr}_u^{\text{W-in}}} + \underbrace{\tfrac{1}{2}\left(1-\tfrac{5}{16}L_{\mathrm{R}}^{-3}\right)\mathrm{Sr}}_{\mathrm{Rr}_\omega^{\text{W-in}}}, \tag{17}$$

while the wall-induced variation of the drag force is [22]

$$\Delta C_{\mathrm{D}}^{\text{W-in}}(\mathrm{Sr}, L_{\mathrm{R}}) = \underbrace{\left(\tfrac{9}{16}L_{\mathrm{R}}^{-1}-\tfrac{1}{8}L_{\mathrm{R}}^{-3}+\tfrac{45}{256}L_{\mathrm{R}}^{-4}+\tfrac{1}{16}L_{\mathrm{R}}^{-5}\right)\left(1-\tfrac{9}{16}L_{\mathrm{R}}^{-1}+\tfrac{1}{8}L_{\mathrm{R}}^{-3}-\tfrac{45}{256}L_{\mathrm{R}}^{-4}-\tfrac{1}{16}L_{\mathrm{R}}^{-5}\right)^{-1}}_{\Delta C_{\mathrm{D}u}^{\text{W-in}}} - \underbrace{\tfrac{5}{32}\left(L_{\mathrm{R}}^{-2}+\tfrac{9}{16}L_{\mathrm{R}}^{-3}\right)\mathrm{Sr}}_{\Delta C_{\mathrm{D}\omega}^{\text{W-in}}}, \tag{18}$$

where $\Delta C_{\mathrm{D}}^{\text{W-in}}(\mathrm{Sr}, L_{\mathrm{R}}) = (C_{\mathrm{D}}^{\text{W-in}}(\mathrm{Sr}, L_{\mathrm{R}}) - C_{\mathrm{D}0}^{\mathrm{U}}(\mathrm{Re}\to 0))/C_{\mathrm{D}0}^{\mathrm{U}}(\mathrm{Re}\to 0)$, with $C_{\mathrm{D}0}^{\mathrm{U}}(\mathrm{Re}\to 0) = 24/\mathrm{Re}$ the drag coefficient in the creeping flow limit. Since the leading contribution of the particle rotation to the drag force is known to be proportional to $L_{\mathrm{R}}^{-4}\mathrm{Rr}$ [38], the above $O(L_{\mathrm{R}}^{-5}) - O(L_{\mathrm{R}}^{-3}\mathrm{Sr})$ approximation for $\Delta C_{\mathrm{D}}^{\text{W-in}}(\mathrm{Sr}, L_{\mathrm{R}})$ also holds for a nonrotating sphere.

When the wall lies in the outer region of the disturbance, the relative length scales L_u, L_ω, and L_Ω are no longer small. Hence, in addition to L_{R}, the drag and lift forces depend on these three visco-inertial length scales. This situation was investigated in the shearless nonrotating case ($L_\omega \to 0$, $L_\Omega \to 0$) in [14], neglecting the finite size of the particle. The relevant solutions were obtained in the form of double integrals which can be approximated as [31]

$$\frac{16}{9}L_{\mathrm{R}}\Delta C_{\mathrm{D}u}^{\text{W-out}}(\mathrm{Re}\lesssim 1) = f_{\mathrm{D}}'(L_u) \approx \frac{1}{1+0.16L_u(L_u+4)} \tag{19}$$

and

$$\frac{8}{9}C_{Lu}^{\text{W-out}}(\text{Re} \lesssim 1) = f_L'(L_u) \approx \begin{cases} [1 + 0.13L_u(L_u + 0.53)]^{-1} & \text{for} \quad L_u \leqslant 10, \\ 7.95L_u^{-2.09} & \text{for} \quad L_u > 10, \end{cases} \tag{20}$$

with $\Delta C_{Du}^{\text{W-out}}(\text{Re} \ll 1) = (C_{Du}^{\text{W-out}}(L_u, L_R) - C_{D0}^{U}(\text{Re} \to 0))/C_{D0}^{U}(\text{Re} \to 0)$. The two functions f_D' and f_L' describe how the wall-induced drag modification and the transverse force decay as inertial effects in the bulk become dominant compared to the wall influence.

In the presence of shear, the case of a nonrotating sphere close to a wall standing in the outer region of the disturbance was worked out in [19]. Again, the solution was obtained in the form of a volume integral in Fourier space. The value of this integral cannot be obtained in closed form but was tabulated for various values of L_ω and $\varepsilon = \widetilde{L}_u/\widetilde{L}_\omega$. These results were fitted in [20] to obtain tractable estimates of the lift force. This fit was further modified in [31] to take into account the effects of the finite particle size, which tend to lower the transverse force when the particle gets very close to the wall. The same argument was used to derive an empirical expression for the drag variation. Making use of the approximate expressions (7) and (8) for $C_{L\omega}^{U}(\text{Re} \ll 1)$ and of the asymptotic form for $C_{Lu}^{\text{W-in}}$ in (15), the final expression for the lift force in the case of a nonrotating sphere takes the form

$$C_L^{W}(\text{Re} \lesssim 1) \approx f_L(L_\omega, \varepsilon) f_L'(L_u) C_{Lu}^{\text{W-in}} + h_L(L_\omega, \varepsilon) C_{L\omega}^{U}(\text{Re} \ll 1), \tag{21}$$

with $f_L'(L_u)$ as given in (20) and

$$f_L(L_\omega, \varepsilon) = e^{-0.22\varepsilon^{0.8}L_\omega^{2.5}} \quad \text{and} \quad h_L(L_\omega, \varepsilon) = 1 - e^{-\frac{11}{96}\pi^2 \frac{L_\omega}{f_L(\varepsilon)}(1 + \frac{17}{48}L_R^{-1} + 0.643L_R^{-2} - 0.280L_R^{-3})}. \tag{22a,b}$$

Due to these empirical prefactors, (21) approaches the inner solution (15) when $L_u \to 0$ and $L_\omega \to 0$, with the exception of the Sr^2-term, usually much smaller than the Sr-term as far as $|\text{Sr}| \lesssim 1$. Similarly, making use of (18) and (19), the total slip-induced near-wall correction to the drag taking into account the finite size of the sphere may be approximated as

$$\Delta C_D^{W}(\text{Re} \lesssim 1) \approx f_D'(L_u) \Delta C_D^{\text{W-in}}. \tag{23}$$

C. Approximate expression for the slip-induced transverse force in a fluid at rest at moderate-to-large Re

No theoretical solution for the hydrodynamic forces can be found when inertial effects are dominant. However, reliable empirical extensions of the low-Reynolds-number predictions may be achieved based on accurate data. Several experimental and numerical studies [15–17] examined the motion of a rigid sphere close to a wall in a quiescent fluid. They revealed that the transverse force exhibits a faster decay with increasing L_u than predicted by the low-but-finite Re solution. In [15], experimental observations were performed with fully contaminated spherical bubbles rising near a wall in a liquid at rest under conditions $\text{Re} \lesssim 100$; such bubbles behave essentially as rigid torque-free spheres. Theoretical considerations about the nature of the particle-wall interaction were summarized through the semiempirical expression for the transverse force coefficient

$$C_{Lu}^{W}[\text{Re} = O(1 - 100)] \approx a^2(\text{Re})(L_R/3)^{g(\text{Re})} C_{Lu}^{\text{W-out}}(\text{Re} \lesssim 1), \tag{24}$$

with

$$a(\text{Re}) = 1 + 0.6\text{Re}^{0.5} - 0.55\text{Re}^{0.08} \quad \text{and} \quad g(\text{Re}) = -2.0 \tanh(0.01\text{Re}). \tag{25a,b}$$

IV. FLOW FIELD AND FUNDAMENTAL MECHANISMS

A. Nonrotating sphere

Figure 2(a) shows how the distribution of the streamwise velocity disturbance along the line ($y = 0$, $z = 0$) perpendicular to the wall, i.e., the x-axis, varies with flow conditions in the case of a sphere translating in a stagnant fluid. The sphere leading the fluid, U_{rel} is negative, so that

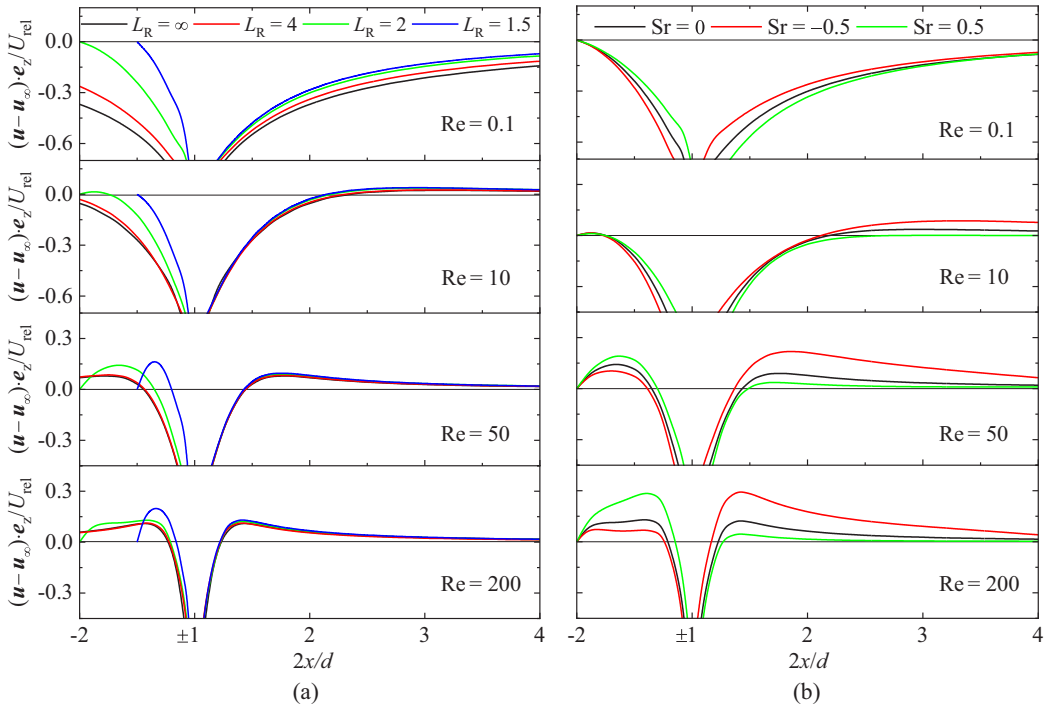

FIG. 2. Distribution of the streamwise velocity disturbance $(\boldsymbol{u} - \boldsymbol{u}_\infty) \cdot \boldsymbol{e}_z/U_{\rm rel}$ along the x-axis (to magnify the flow in the gap, the $]-1,+1[$ part of the axis has been cut, so that the sphere is shrunk to a point). (a) Stagnant fluid (Sr = 0) for different separation distances; (b) linear shear flow for $L_{\rm R} = 2$. The wall stands at $2x/d = -1.5$, -2, and -4 for $L_{\rm R} = 1.5$, 2, and 4, respectively. In (a), the fluid domain has arbitrarily been cut on the left at $x/d = -1$ irrespective of $L_{\rm R}$; the black lines ($L_{\rm R} = \infty$) on the left and right of the particle are of course symmetric.

negative (positive) normalized velocities correspond to an upward (downward) fluid motion. At high Reynolds number (Re = 200), the no-slip condition induces a thin boundary layer around the sphere, within which the disturbance is always negative. Outside this boundary layer, the fluid is accelerated by the sphere motion, making the disturbance become positive on both sides. Owing to the finite-gap offered to the fluid, this acceleration is more pronounced on the wall-facing side and the maximum velocity increases as the wall-sphere separation decreases. In this high-Re configuration, the velocity disturbance outside the boundary layer remains positive throughout the gap. Wall-proximity effects sharply decrease as the gap widens and are almost negligible for $L_{\rm R} \gtrsim 4$, which results in a left-right symmetry of the streamwise velocity distribution in Fig. 2(a). The boundary layer thickens as Re decreases and viscous effects increasingly control the flow in the gap. For instance, the velocity disturbance keeps a negative sign throughout the gap for $L_{\rm R} = 1.5$ when Re = 10, and passes through only a tiny positive maximum for $L_{\rm R} = 2$ before returning to zero at the wall. In such cases, the fluid in the gap is essentially entrained by the sphere translation. For each $L_{\rm R}$, the velocity disturbance at a given distance from the sphere surface is seen to reach larger negative values on the wall-facing side compared to the "free" side, illustrating the enhancement of viscous effects in the gap due to the nearby wall.

The influence of the shear on the disturbance flow is illustrated in Fig. 2(b), based on the results obtained with two opposite relative shear rates, Sr = ± 0.5, for a separation distance $L_{\rm R} = 2$. In the moving frame, the presence of a positive (negative) shear, corresponding to the configuration where the sphere lags (leads) the fluid, accelerates (decelerates) the flow on the wall-facing side,

while it decelerates (accelerates) it on the opposite side. Consequently, compared to the unsheared situation, the fluid acceleration is enhanced (reduced) on the wall-facing side by a positive (negative) shear when Re is large [Re = 100 or 200 in Fig. 2(b)], while the opposite takes place on the "free" side. At moderate Reynolds number (Re = 10), shear-induced acceleration and deceleration effects remain significant within the boundary layer and extend beyond it ($x/d > 1$) on the "free" side. The shear-induced asymmetry is still present throughout the flow at low Reynolds number (Re = 0.1), the disturbance velocity remaining negative everywhere (i.e., directed upstream of the local carrying flow) in this case.

The distribution of the spanwise component of the vorticity disturbance in the symmetry plane $y = 0$ is displayed in Fig. 3 for the specific separation $L_R = 2$. Vorticity is generated both at the sphere surface and at the wall, owing to the no-slip condition on both surfaces. We refer to the corresponding two contributions in the vorticity field as the "surface" vorticity and "wall" vorticity, respectively. When the fluid is at rest at infinity, the surface vorticity is advected asymmetrically, preferentially towards the wall at high Reynolds number [Fig. 3(k)]. A thin layer of wall vorticity, the strength of which increases with Re, takes place in the lower part of the gap. In the same panel, it may be noticed that the stagnation point at the back of the sphere stands slightly below the plane $x = 0$, i.e., it is shifted towards the wall compared to unbounded flow configuration, in agreement with previous observations [16]. When the Reynolds number decreases, the thickness of the two boundary layers increases [e.g., Re = 50 in Fig. 3(h)], reinforcing their interaction. At lower Reynolds number [Re = 10 and 0.1; Figs. 3(e) and 3(b)], diffusion in the crosswise (x) direction is sufficiently efficient to allow the surface vorticity to control the wall region, except in the narrowest part of the gap ($|z|/d \ll 1$). In this regime, the vorticity distribution is essentially similar to that observed in [31] with a spherical bubble, up to a factor 3/2 resulting from the difference in the magnitude of the Stokeslet (hence the drag force) associated with the two types of bodies. Thus, the mechanisms responsible for the drag enhancement and the transverse force are similar to those discussed in [31]. In particular, the gradual slowing down of the fluid displaced by the sphere along the wall as the downstream distance increases induces a small transverse flow correction directed away from the wall, which is responsible for the repulsive transverse force acting on the sphere.

In the presence of an ambient shear, a shear-flow type correction has to take place within the boundary layer for the no-slip condition to be satisfied at the sphere surface, yielding a negative correction in the spanwise vorticity therein when the sphere lags the fluid. Hence this correction enhances the primary negative vorticity on the "free" side ($x > 0$), while it lowers the primary positive vorticity in the part of the boundary layer facing the wall ($x < 0$), as Fig. 3(i) confirms. The process reverses when the sphere leads the fluid, in agreement with Fig. 3(g). The wall vorticity in the gap is also modified by the shear: it increases (decreases) for Sr > 0 (Sr < 0), owing to the acceleration (deceleration) of the fluid on the wall-facing side caused by the positive (negative) shear, as Figs. 3(l) and 3(j) confirm.

The near-wall configuration makes the flow past the sphere intrinsically three-dimensional, even when the fluid is at rest at infinity. Consequently, the streamwise component of the vorticity, $\omega_z = \boldsymbol{\omega} \cdot \boldsymbol{e}_z$, is nonzero in the wake, unlike the axisymmetric configuration prevailing in the unbounded case at low and moderate Re. The ω_z-distribution in the unsheared case is shown in Figs. 4(b) and 4(e) at Re = 200 for the two separations $L_R = 1.5$ and $L_R = 2.0$, respectively. The streamwise vorticity is concentrated within two elongated vortices standing on both sides of the symmetry plane $y = 0$. The fluid located in between the two vortex threads is entrained downwards, bending the isocontours of the spanwise vorticity towards the wall, as seen in Fig. 3(k). Three-dimensional effects sharply decrease as L_R increases, and so does the strength of ω_z as shown by Fig. 4(e). In an unbounded flow, the axial symmetry in the wake of a sphere is known to break down at a critical Reynolds number $\mathrm{Re}^{SS} \approx 212.6$ through a stationary bifurcation [33,41], leading to a stationary flow with a double-threaded wake structure qualitatively similar to that depicted in Fig. 4(b), and a symmetry plane whose orientation is selected by some initial disturbance. In the presence of a nearby wall, the flow structure observed for $\mathrm{Re} \gtrsim \mathrm{Re}^{SS}$ results from the combination of the above two mechanisms, the presence of the wall dictating the orientation of the symmetry plane [16]. The

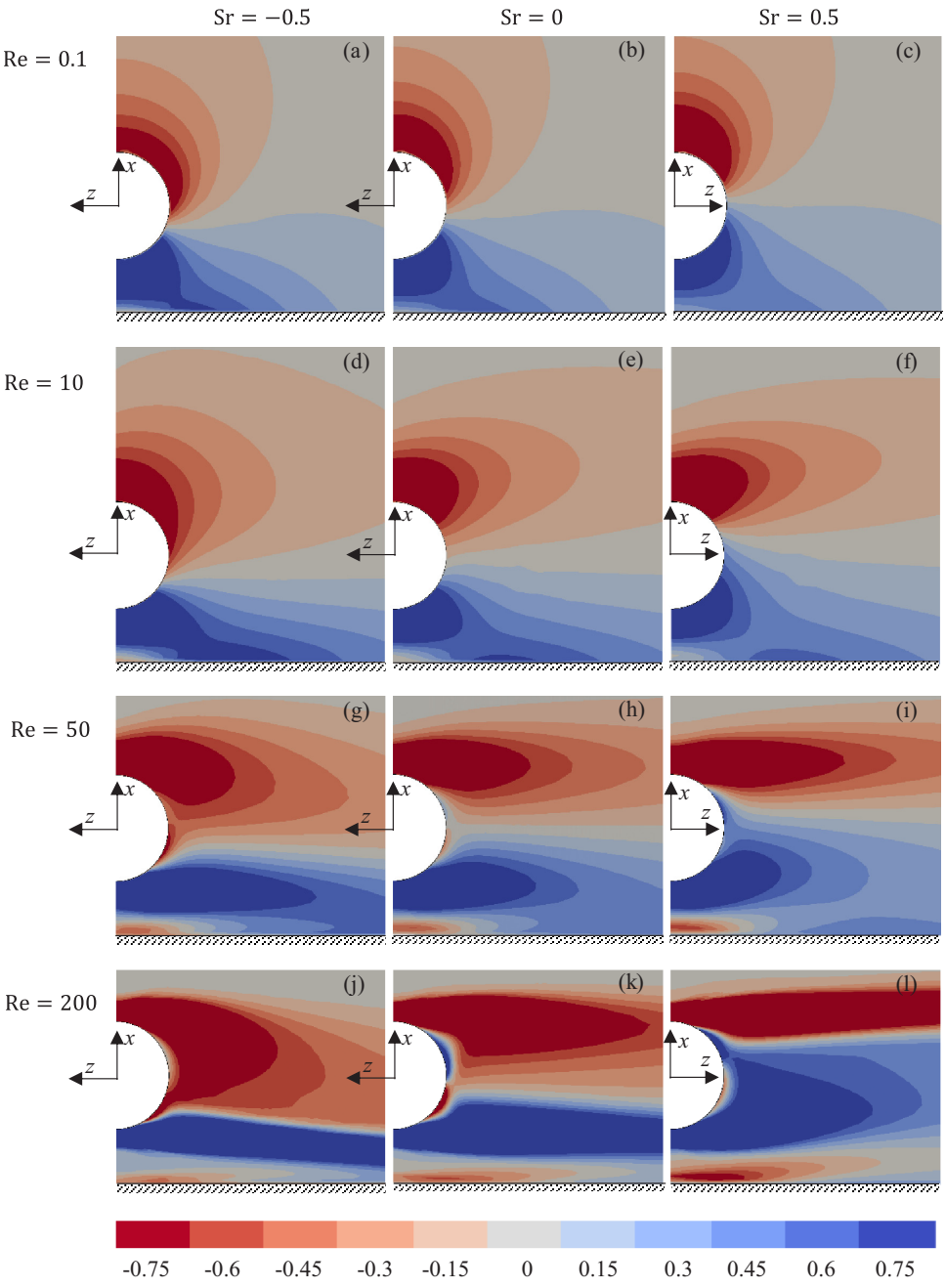

FIG. 3. Isocontours of the normalized spanwise vorticity disturbance $d/(2U_{\mathrm{rel}})(\boldsymbol{\omega}-\boldsymbol{\omega}_\infty)\cdot\boldsymbol{e}_y$ in the symmetry plane $y=0$ for $L_{\mathrm{R}}=2$. Left column: $\mathrm{Sr}=-0.5$ ($U_{\mathrm{rel}}<0$); central column: $\mathrm{Sr}=0$ ($U_{\mathrm{rel}}<0$); right column: $\mathrm{Sr}=0.5$ ($U_{\mathrm{rel}}>0$). The wall stands at the bottom of each panel. The relative flow with respect to the sphere is from left to right, i.e., in the z-direction for $\mathrm{Sr}=0.5$ and in the $-z$-direction for $\mathrm{Sr}=0$ and -0.5.

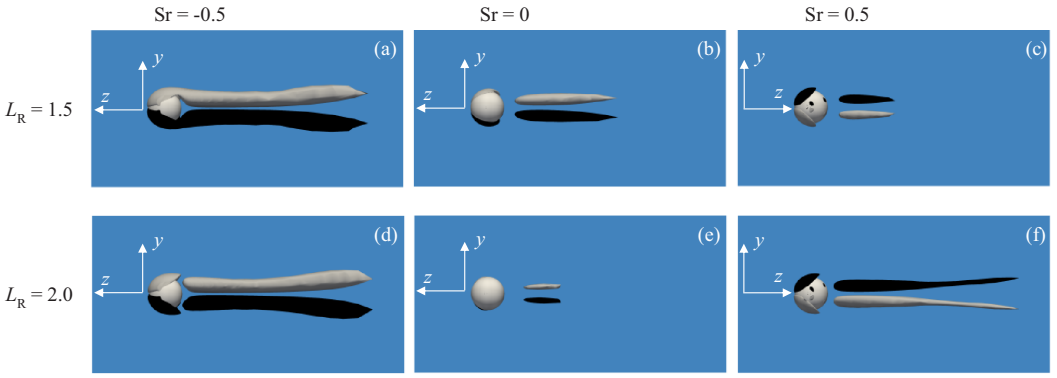

FIG. 4. Isosurfaces $d/(2|U_{\rm rel}|)\boldsymbol{\omega}\cdot\boldsymbol{e}_z = \pm 0.25$ of the streamwise vorticity in the wake of a sphere moving parallel to a wall at Re = 200 (the black thread corresponds to positive values). Left column: Sr = −0.5 ($U_{\rm rel} < 0$); central column: Sr = 0 ($U_{\rm rel} < 0$); right column: Sr = 0.5 ($U_{\rm rel} > 0$). The flow with respect to the sphere is from left to right, i.e., in the z-direction for Sr = 0.5, and in the $-z$-direction for Sr = 0 and −0.5. Since (x, y, z) is right-handed, the wall stands at the back of the sphere for Sr = 0.5 and in front of it for Sr = 0 and −0.5.

corresponding wake structure is illustrated in Fig. 5(e) for Re = 250 and two separations, $L_R = 1.5$ and 8. Now, the strength of the streamwise vortices is significant even for $L_R = 8$, owing to the intrinsic instability of the axisymmetric wake. At such large separations and Reynolds number, the sign of the streamwise vorticity in each vortex thread is dictated by the slight acceleration of the fluid in the gap: based on Bernoulli's theorem, this acceleration is seen to imply a pressure minimum there, forcing the fluid located within the symmetry plane $y = 0$ (i.e., in between the two streamwise vortices) to be deviated toward the wall. Continuity then implies that the fluid must go away from the wall on the outer side of the streamwise vortices, yielding a transverse force toward $x > 0$. Consequently, the wall-interaction and the intrinsic wake instability mechanisms cooperate when the separation distance decreases, enhancing the strength of the streamwise vortices, as the comparison between Fig. 5(b) and Figs. 5(e) and 4(b) confirms.

In the presence of a mean shear, the "free" vorticity $\boldsymbol{\omega}_\infty = \nabla \times \boldsymbol{u}_\infty = -\gamma \boldsymbol{e}_y$ comes into play. In an unbounded flow domain, it yields the classical shear-induced lift force associated with the lift coefficient (7) in the low-Re regime. In the case of a rigid nonrotating sphere, a remarkable feature is that this force changes sign for Re $\gtrsim$ 50 [9,11], mostly because of the nearly uniform shear stress

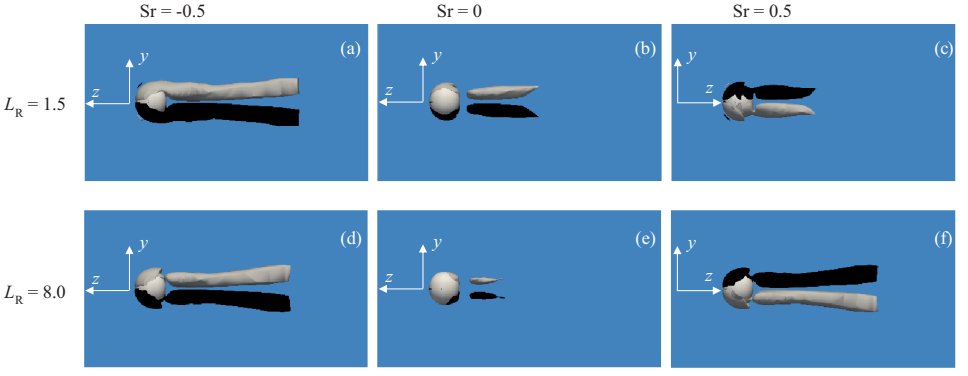

FIG. 5. Same as Fig. 4 for Re = 250.

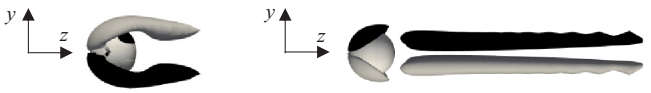

FIG. 6. Isosurfaces of the streamwise vorticity in the wake of a sphere moving in an unbounded linear shear flow with Sr = 0.5 (the black thread corresponds to the positive value). (a) Re = 50, $d/(2|U_{\rm rel}|)\boldsymbol{\omega}\cdot\boldsymbol{e}_z = \pm 0.1$; (b) Re = 200, $d/(2|U_{\rm rel}|)\boldsymbol{\omega}\cdot\boldsymbol{e}_z = \pm 0.25$. The relative upstream flow is from left to right, and the free vorticity $-\gamma$ lies along the y-direction.

distribution within the recirculation attached to the rear part of the sphere. This change of sign, which follows that of the streamwise vorticity within each vortex thread, is confirmed in Fig. 6. In the presence of a nearby wall, a consequence of this change of sign is that, provided Re $\gtrsim$ 50, the shear-induced and slip-induced mechanisms cooperate when Sr is negative and act in an antagonistic manner when Sr is positive, while the reverse happens for Re $\lesssim$ 50. The influence of the sign of Sr in the former case is confirmed in Fig. 4 (Re = 200), since the trailing vortices observed when Sr < 0 [Figs. 4(a) and 4(d)] are thicker than in the unbounded case [Fig. 6(b)], while they are thinner when Sr > 0 [Figs. 4(c) and 4(f)].

The presence of the double-threaded wake and the variation of its strength with the sign of Sr have a direct influence on the advection of the surface vorticity downstream of the sphere. Indeed, according to the direction of the streamwise vorticity in each vortex thread, this wake structure entrains the fluid standing close to the midplane $y = 0$ towards (away from) the wall when Sr < 0 (Sr > 0). Since the streamwise vortices are stronger in the former case, so is the resulting bending of the wake towards the wall [Fig. 3(j)], as compared to its bending toward the fluid interior when Sr is positive [Fig. 3(l)].

For supercritical Reynolds numbers, i.e., Re $>$ Re^{SS}, the above picture still holds when Sr is negative, since all mechanisms involved in the generation of the streamwise vorticity cooperate. The only difference is that the magnitude of ω_z is increased compared to subcritical conditions, since the wake instability contributes to reinforce this vorticity component [compare the diameters of the ω_z isosurfaces corresponding to Re = 200 and 250 in Figs. 4(a) and 5(a)]. In contrast, when Sr is positive, the mechanism associated with the free vorticity and those related to the wall proximity and wake instability act in an antagonistic manner. Therefore, the resulting sign of the streamwise vorticity in each vortex thread depends on the magnitude of Sr. For large enough relative shear rates, this sign follows that found in the unbounded configuration. As the comparison between Figs. 5(c) and 6(b) shows, this is the case with Sr = 0.5 at Re = 250. In contrast, mechanisms related to the wall proximity and wake instability dominate when the ambient shear is weak enough. This situation is illustrated in Fig. 7(b) (Sr = 0.2), where the sign of ω_z in each vortex thread is seen to be opposite to that found in Fig. 5(c) with Sr = 0.5 at the same Reynolds number and separation from the wall.

As the Reynolds number decreases, shear-induced advective effects in the wake weaken and vorticity diffusion across the wall-particle gap becomes increasingly important. For instance, bending of the surface vorticity toward or away from the wall is no longer observed in Figs. 3(g)–3(i) at Re = 50. At Re = 10, the boundary layer is thick enough for the positive vorticity disturbance

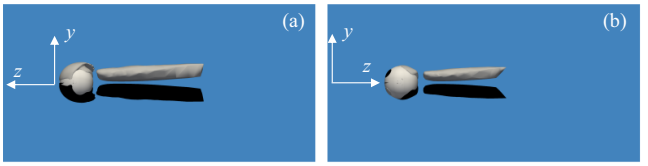

FIG. 7. Same as Figs. 5(a) and 5(c) for Sr = $\pm$0.2.

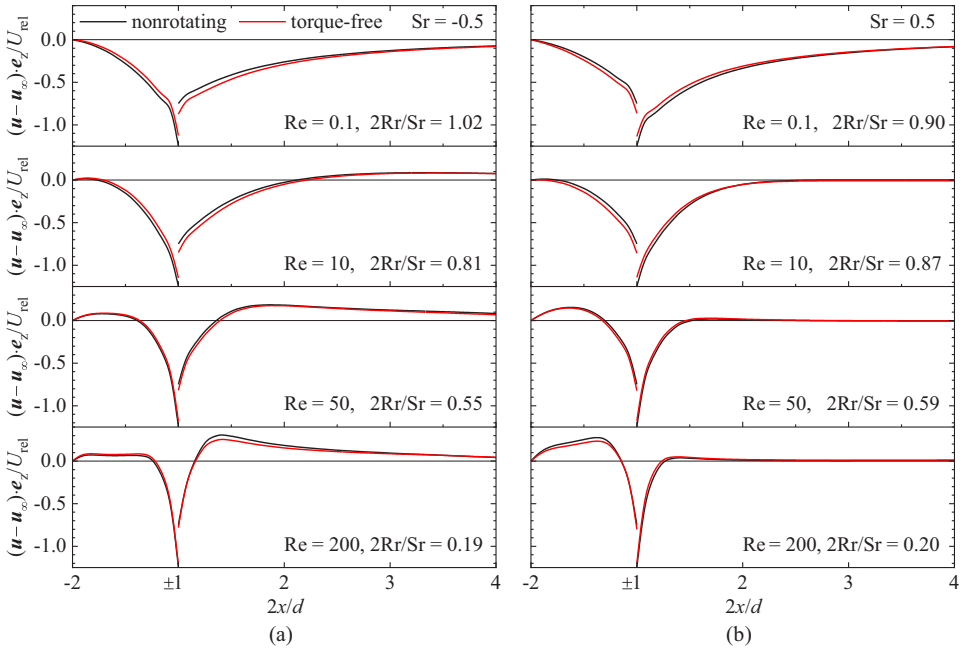

FIG. 8. Influence of the sphere rotation on the distribution of the streamwise velocity disturbance $(\boldsymbol{u}-\boldsymbol{u}_\infty)\cdot\boldsymbol{e}_z/U_{\rm rel}$ along the x-axis for $L_{\rm R}=2$. (a) Sr $=-0.5$; (b) Sr $=0.5$. The wall stands at position $2x/d=-2$, and the interval $]-1,+1[$ has been cut. The magnitude of the normalized sphere rotation rate $2{\rm Rr}/{\rm Sr}=2\Omega/\gamma$ in the torque-free case is indicated in each panel.

generated on the wall-facing part of the sphere surface to interact directly with the negative wall vorticity disturbance, similar to the unsheared case. As Re further decreases, viscous diffusion becomes so strong that the surface vorticity virtually controls the entire wall region. Nevertheless, influence of the ambient shear is still present, favoring (reducing) the diffusion of the surface vorticity toward the wall when Sr is negative (positive), as the isocontours in Figs. 3(a)–3(c) reveal. The surface vorticity being enhanced (reduced) on the wall-facing side for negative (positive) Sr, the drag acting on the sphere is increased (reduced), which is reflected in the last term in the right-hand side of (18). The wall- and shear-induced mechanisms both yield a transverse force directed toward $x>0$ if Sr is positive in the low-but-finite Re regime. Hence they act together to produce an enhanced repulsive force in this configuration, as reflected in (15), whereas their antagonistic action yields a reduced transverse force when Sr is negative.

B. Torque-free sphere

Figure 8 compares the profiles of the streamwise velocity disturbance along the x-axis in the case of a torque-free sphere with that of a nonrotating sphere, both with Sr $=\pm0.5$ and $L_{\rm R}=2$. Values of the normalized rotation velocity $2{\rm Rr}/{\rm Sr}=2\Omega/\gamma$ indicated in each panel reveal a significant decrease of the rotation rate as Re increases, Rr typically reducing by a factor of five from Re $=0.1$ to Re $=200$. A similar tendency has been reported in the unbounded case [11,42]. Rotation being clockwise for Sr >0, the streamwise velocity is found to decrease on the wall-facing side and increase on the opposite side; the reverse happens when Sr is negative. However, the corresponding changes are minimal and vanish beyond a distance to the sphere surface of the order of its radius. Analyzing the spatial distribution of the spanwise vorticity disturbance (not shown) leads to the same conclusion.

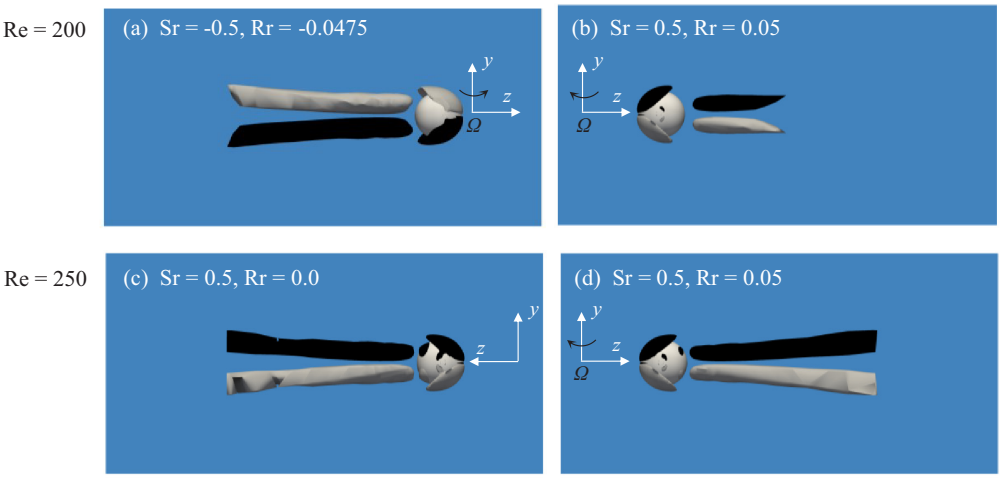

FIG. 9. Isosurfaces $d/(2|U_{\rm rel}|)\boldsymbol{\omega}\cdot\boldsymbol{e}_z = \pm 0.25$ of the streamwise vorticity around a torque-free sphere for $L_{\rm R} = 2$ and $|{\rm Sr}| = 0.5$.

Things differ at high Reynolds number for the streamwise vorticity component. Figure 9 shows the structure of the ω_z-field in the wake of a torque-free sphere for ${\rm Sr} = \pm 0.5$ and a separation distance $L_{\rm R} = 2$. The aforementioned rotation-induced changes in the fluid velocity at the particle surface lower the actual shear "felt" by the sphere whatever the sign of Sr. Therefore the source term responsible for the generation of the streamwise vorticity is lowered by the rotation, resulting in a weaker pair of vortex threads compared to the nonrotating configuration. Comparing Fig. 9 with its counterpart in the case of a nonrotating sphere [Figs. 4(d) and 4(f)] confirms this conclusion. In contrast, under supercritical conditions, the generation of ω_z for similar levels of $|{\rm Sr}|$ is essentially governed by the wake instability, not by the shear around the particle. Consequently, little change is expected between the nonrotating and torque-free configurations, which Figs. 9(c)–9(d) confirm.

V. HYDRODYNAMIC FORCES

We now discuss the variations of the computed drag and lift forces acting on the sphere with the various control parameters. Most results were obtained by considering the parameter range $0.1 \leqslant {\rm Re} \leqslant 250$ and $|{\rm Sr}| \leqslant 0.5$, within which the flow field in the particle frame is steady for all considered $L_{\rm R}$. Numerical data are systematically used to derive empirical or semiempirical force models. Most of these models are valid only within a specific Re range but we frequently combine them to obtain empirical fits valid throughout the considered range of Reynolds number.

A. Fluid at rest at infinity

1. Drag

It is known since Faxén's pioneering work [43] that the presence of a wall increases the drag in the low-Re limit. This increase, say, $\Delta C_{{\rm D}u}^{\rm W} = (C_{{\rm D}u}^{\rm W} - C_{\rm D0}^{\rm U})/C_{\rm D0}^{\rm U}$, with $C_{\rm D0}^{\rm U}$ the drag coefficient on a sphere translating in an unbounded uniform flow, is displayed for various separation distances in Fig. 10, the two panels of which focus on the Reynolds number ranges $0.1 \leqslant {\rm Re} \leqslant 20$ and $100 \leqslant {\rm Re} \leqslant 250$, respectively. Data for the wall-induced drag increase extracted from [16] and [29], both for a nonrotating sphere, are also included. Since these references provide $C_{{\rm D}u}^{\rm W}$ but not $C_{\rm D0}^{\rm U}$, we used our own results for the latter to compute $\Delta C_{{\rm D}u}^{\rm W}$. This procedure introduces some uncertainty because $\Delta C_{{\rm D}u}^{\rm W}$ is small in most cases and may therefore be sensitive to a small difference in $C_{\rm D0}^{\rm U}$. For instance, a 2% decrease in $C_{\rm D0}^{\rm U}$ makes the data of [29] collapse perfectly on present results at

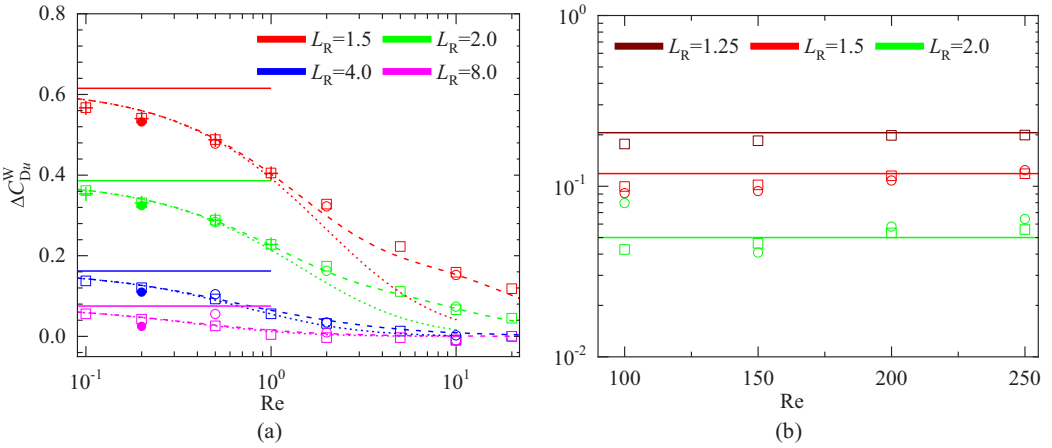

FIG. 10. Relative wall-induced drag increase ΔC_{Du}^{W} for a sphere moving parallel to a wall in a fluid at rest. (a) Low-to-moderate-Re regime. (b) High-Re regime. □ and +: numerical data corresponding to a nonrotating and a torque-free sphere, respectively; ○ and •: numerical data from [16] and [29], respectively; solid lines in (a): zero-Re asymptotic prediction (18); dotted lines: low-but-finite-Re prediction (23); dashed lines: low-to-moderate-Re semiempirical prediction (27); solid lines in (b): high-Re expression (28).

$\mathrm{Re} = 0.2$. Despite this uncertainty, the estimates for ΔC_{Du}^{W} obtained through the above procedure are found to be in good agreement with present predictions whatever L_R and Re. Most results from the present investigation presented in Fig. 10(a) were obtained by considering a nonrotating sphere but data corresponding to the torque-free condition are also included for $\mathrm{Re} \leqslant 1$. No discernible difference is found between the two configurations, confirming the vanishingly small effect of the rotation induced by the torque-free condition on the drag in the range of separations considered here, in line with a previous remark on the asymptotic prediction (18). Numerical results closely approach this prediction [solid lines in Fig. 10(a)] at $\mathrm{Re} = 0.1$. Inertial effects become increasingly important as the Oseen-length-based separation L_u increases, making the drag increase depart from (18). The decrease in ΔC_{Du}^{W} as Re increases is well captured by the low-but-finite-Re expression (23) up to $\mathrm{Re} = 1$. Following [15], this expression may be extended semiempirically to moderate Reynolds numbers by noting that the drag increase in this regime is proportional to the square of the maximum surface vorticity. Variations of this quantity with Re based on the results of [44] are expressed by the fitting function $a(\mathrm{Re})$ in (25a). We performed specific runs in an unbounded uniform flow to check this expression and found that, for $\mathrm{Re} \lesssim 10$, these variations are more accurately approached by the fit $a(\mathrm{Re}) \approx (1 - 0.12\mathrm{Re}^{1/2} + 0.37\mathrm{Re})^{1/2}$ which recovers the leading-order $0.6\mathrm{Re}^{1/2}$ term of (25a) at high Reynolds number. However, compared with the unbounded situation, the presence of a nearby wall tends to decrease the surface vorticity on the wall-facing side, as Fig. 3(e) indicates. For this reason, we found that a more accurate estimate of the variations of the maximum surface vorticity in the near-wall configuration at moderate Re is provided by

$$a^{W}(\mathrm{Re}, L_R) \approx \left\{1 + \tanh\left(0.05\mathrm{Re}L_R^2\right)(0.37\mathrm{Re} - 0.12\mathrm{Re}^{1/2})\right\}^{1/2}. \tag{26}$$

Making use of (26), which tends toward the above expression for $a(\mathrm{Re})$ at large distances from the wall, the low-but-finite-Re wall-induced drag correction (23) may be extended toward moderate Reynolds numbers in the form

$$\Delta C_{Du}^{W}[\mathrm{Re} \lesssim 10)] \approx f_D'(L_u)[a^{W}(\mathrm{Re}, L_R)]^2 \Delta C_{Du}^{W\text{-in}}(L_R), \tag{27}$$

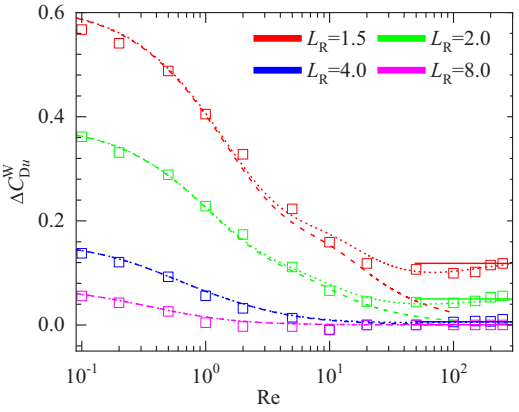

FIG. 11. Wall-induced drag correction ΔC_{Du}^{W} for a nonrotating sphere translating parallel to a wall in a fluid at rest in the range $0.1 \leqslant \mathrm{Re} \leqslant 250$. Symbols: numerical data; solid lines: high-Re correction (28); dashed lines: low-to-moderate-Re correction (27); dotted lines: composite fit (29).

where $\Delta C_{Du}^{W\text{-in}}$ corresponds to the low-Re asymptotic prediction (18) for $\mathrm{Sr} = 0$ and f'_D is given by (19). As the dashed lines in Fig. 10(a) show, (27) accurately captures the variations of ΔC_{Du}^{W} revealed by the simulations whatever L_R up to $\mathrm{Re} = 20$.

According to (27), the wall-induced drag increase should be vanishingly small beyond $\mathrm{Re} \approx 100$. However, as Fig. 10(b) reveals, numerical data in this regime indicate that this increase is still significant when the particle is close enough to the wall. Within the considered Reynolds number range ($100 \leqslant \mathrm{Re} \leqslant 250$), this increase is found to depend only weakly on Re. In contrast, it varies dramatically with the inverse of the separation distance, increasing from 5% for $L_R = 2$ to 20% for $L_R = 1.25$. Fitting the results corresponding to $\mathrm{Re} = 250$ yields

$$\Delta C_{Du}^{W}[\mathrm{Re} = O(100)] \approx 0.4 L_R^{-3}. \tag{28}$$

Figure 10(b) shows that (28) captures the observed drag increase well for $\mathrm{Re} \gtrsim 100$. The -3 exponent in (28) is readily understood by noting that there is little direct interaction between the near-sphere and near-wall vortical regions in this regime [see Fig. 3(k)]. Therefore, the sphere-wall interaction has an almost inviscid nature, meaning that the sphere perceives the wall essentially as a free-slip plane and the latter perceives the sphere as an irrotational dipole (associated with its finite size). The image dipole required to satisfy the nonpenetration condition on a nearby plane is known to induce an $O(L_R^{-3})$ increase in the relative velocity of the fluid at the sphere center, which in turn increases the viscous dissipation resulting from the sphere motion by a similar amount [45]. Equating the dissipation rate with the rate of work of the drag force then implies that ΔC_{Du}^{W} is proportional to L_R^{-3}.

Figure 11 compares the predictions provided by expressions (27) and (28) with the numerical data obtained throughout the Re range investigated. Obviously none of them is appropriate in the intermediate range $20 \lesssim \mathrm{Re} \lesssim 100$. For practical purposes, an empirical fit resulting from the combination of the two models is desirable. Noting that the drag excess predicted by (27) becomes vanishingly small when the Reynolds number exceeds a few tens, a linear combination of (27) and (28) with a suitable prefactor in the latter ensuring that its effect vanishes at low Reynolds number appears to be convenient. Calibrating this prefactor in the intermediate Re range, we obtained

$$\Delta C_{Du}^{W}(\mathrm{Re}) \approx \Delta C_{Du}^{W}[\mathrm{Re} \lesssim 10] + c_{Du\infty}(\mathrm{Re}) \Delta C_{Du}^{W}[\mathrm{Re} = O(100)], \quad \text{with}$$
$$c_{Du\infty}(\mathrm{Re}) = 1 - e^{-0.035 \mathrm{Re}^{0.75}}. \tag{29a,b}$$

As the dotted lines in Fig. 11 show, this composite expression correctly reproduces the observed wall-induced drag increase whatever the Reynolds number.

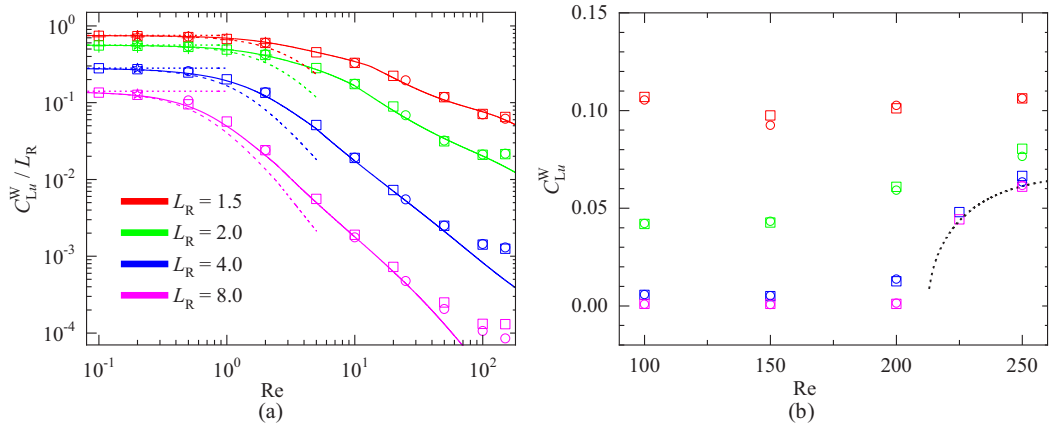

FIG. 12. Lift coefficient [divided by L_R in (a) for a better readability] on a sphere translating parallel to a wall in a fluid at rest. (a) Regime $0.1 \leqslant \mathrm{Re} \leqslant 100$. (b) high-Re regime $\mathrm{Re} \geqslant 100$. □ and +: present numerical data for a nonrotating and a torque-free sphere, respectively; ○ and ☆: numerical data from [16] and [29], respectively; dotted lines in (a): leading-order term of asymptotic expressions (15) and (16); dashed lines: approximate low-but-finite Re expression (20); solid lines: low-to-moderate Re prediction (24) with $a(\mathrm{Re})$ substituted with $a^W(\mathrm{Re})$ as given by (26); dotted line in (b): prediction (30) for the lift force in an unbounded fluid beyond the stationary bifurcation.

2. Transverse force

Numerical data obtained for the wall-induced transverse force are displayed in Fig. 12. Data from [16] for a nonrotating sphere are also included. The two sets of results are found to be in excellent agreement throughout the explored parameter space. Close to the low-Re bound of the domain ($\mathrm{Re} = 0.2$), present results are compared with those of [29]. Again a very good agreement is observed. Figure 12(a) shows the transverse force coefficient in the range $0.1 \leqslant \mathrm{Re} \leqslant 150$. Most data correspond to a nonrotating sphere, but some of them, obtained at small wall distances and Reynolds numbers less than unity, correspond to a torque-free sphere. Given the vanishingly small difference between the results corresponding to these two configurations at small Re and the similar behavior observed in the moderate-to-high Re regime in [16], it may be concluded that the sphere rotation associated with the torque-free condition has a negligible effect on the wall-induced transverse force. Although this effect is reflected in the difference among the prefactors involved in (15) and (16), the overall difference between the two predictions amounts only to 0.3% for $L_R = 1.5$ and 0.4% for $L_R = 1.25$, confirming the above statement. Numerical results at $\mathrm{Re} = 0.1$ are in good agreement with these asymptotic predictions, beyond which the transverse force gradually decreases as inertial effects increase, making the wall move from the inner region of the disturbance to the outer region. This decrease is well captured by (20) up to $\mathrm{Re} \approx 1$. Further increasing Re reveals that the force predicted by this low-but-finite Re approximation decreases too fast. A similar trend was noticed in [15], leading to the semiempirical extension (24) of the previous prediction. This extension was obtained by noting that, similar to the wall-induced drag increase, the transverse force at low-to-moderate Re is proportional to the square of the maximum vorticity at the sphere surface, and the dependence of this force with respect to L_u varies from L_u^{-2} for $\mathrm{Re} \lesssim 1$ to L_u^{-4} for $\mathrm{Re} \gg 1$. In [16] and [17], this extended prediction was found to be in good agreement with numerical results up to $L_u = 100$ for $1.5 \leqslant L_R \leqslant 8$. Predictions of (24), with the slight change from $a(\mathrm{Re})$ to $a^W(\mathrm{Re})$ as given in (26) are shown in Fig. 12(a). They are seen to capture the variations of the transverse force well up to $\mathrm{Re} \approx 100$ for $L_R < 4$. At larger L_R, they tend to underestimate the actual force for $\mathrm{Re} \gtrsim 20$. However, under such conditions, the residual values of the force are less than 1% of the low-Re value, making this underestimate of little significance.

Figure 12(b) shows how C_{Lu}^{W} behaves for $\mathrm{Re} \geqslant 100$. For large enough wall-particle separations, typically $L_R \gtrsim 4$, the transverse force is virtually zero up to $\mathrm{Re} \approx 200$. In this situation, the sphere is immersed in an almost uniform flow, so that its wake is essentially axisymmetric. The axial symmetry breaks down when the Reynolds number exceeds the critical value $\mathrm{Re} = \mathrm{Re}^{SS}$, giving rise to a nonzero transverse force at larger Reynolds numbers. The wall plays no role in the occurrence of this force, nor in its intensity. However, it selects the orientation of the symmetry plane that characterizes the wake beyond the threshold Reynolds number, hence that of the transverse force, according to the mechanism discussed in Sec. IV A. The corresponding imperfect bifurcation being supercritical and of pitchfork type [46], it gives rise to a force growing as the square root of $\mathrm{Re} - \mathrm{Re}^{SS}$ close to the threshold. The associated prefactor ($\approx$2.95) was computed exactly through a weakly nonlinear approach in the case of a translating sphere subject to a slow rotation in a fluid at rest, this rotation being responsible for the imperfect nature of the bifurcation [46]. An empirical extension of this prediction to non-negligible $\mathrm{Re} - \mathrm{Re}^{SS}$ gaps was proposed in [37] in the form

$$C_{L}^{\mathrm{Re}>\mathrm{Re}^{SS}} \approx 2.95\left(\frac{\mathrm{Re}^{SS}}{\mathrm{Re}}\right)^{1.5}[(\mathrm{Re}^{SS})^{-1} - \mathrm{Re}^{-1}]^{1/2}. \tag{30}$$

Figure 12(b) shows that present results corresponding to $L_R = 8$ follow closely this prediction up to $\mathrm{Re} = 250$, i.e., nearly 20% beyond the threshold. As the wall-sphere separation decreases, the situation becomes less clear-cut because the flow "felt" by the sphere remains significantly anisotropic, even for $\mathrm{Re} \gtrsim 100$. Hence the transverse force maintains a significant nonzero value throughout the range $100 \lesssim \mathrm{Re} \lesssim \mathrm{Re}^{SS}$. For low enough separations, the force exhibits little variation with the Reynolds number in that range and even up to $\mathrm{Re} = 250$. For instance, C_{Lu}^{W} varies only by $\pm 5\%$ about a mean value close to 0.1 for $L_R = 1.5$. Under such conditions, no stationary bifurcation takes place, the wake structure having reached some kind of "asymptotic" state that breaks down only at much higher Reynolds number with the occurrence of unsteady effects. The case $L_R = 2$ represents an intermediate situation in which the transverse force is seen to increase significantly beyond $\mathrm{Re} = 150$, almost doubling its value at $\mathrm{Re} = 250$. This variation suggests that the wake structure changes significantly within this range. This was confirmed in [16], where it was shown that the size of the double-threaded wake structure grows dramatically from $\mathrm{Re} = 100$ to $\mathrm{Re} = 200$ (their Fig. 12). Since the streamwise vortices act to deflect the fluid toward the wall in the symmetry plane, the wake it more vigorously tilted in that direction as Re increases, a trend confirmed by the comparison of Figs. 3(h) and 3(k). This in turn increases the fluid velocity directed toward the flow interior on the outer side of the streamwise vortices, hence the repelling transverse force.

B. Linear shear flow

1. Drag on a nonrotating sphere

The drag change ratio $\Delta C_{D}^{W} = (C_{D}^{W} - C_{D0}^{U})/C_{D0}^{U}$ is reported in Fig. 13 for different separation distances and dimensionless shear rates. Let us first consider results obtained in the low-to-moderate Reynolds number regime ($0.1 \leqslant \mathrm{Re} \leqslant 20$) with a dimensionless shear rate $\mathrm{Sr} = \pm 0.5$ [Fig. 13(a)]. For $L_R \leqslant 4$, the shear-induced drag modification is negligibly small compared with that resulting from the presence of the wall. In contrast, for the smallest two separations, the shear is found to increase (decrease) the drag when the sphere leads (lags) the fluid, which is supported by the qualitative discussion at the end of Sec. IV A. The asymptotic prediction (18), valid in the low-Re limit provided the wall stands in the inner region of the disturbance, is in good agreement with numerical results at $\mathrm{Re} = 0.1$. Compared with the unsheared case, the corresponding relative variation of ΔC_{D}^{W} is approximately 8% for $\mathrm{Sr} = \pm 0.5$. No explicit theoretical solution for ΔC_{D}^{W} is available for $\mathrm{Sr} \neq 0$ when the wall stands in the outer region of the disturbance. However, the relative influence of the shear is always small under the conditions considered here, and the decrease of ΔC_{D}^{W} up to $\mathrm{Re} = 1$ is satisfactorily captured by (23), as the solid lines in Fig. 13 show. To extend this estimate to Reynolds numbers of $O(10)$, we merely duplicate the arguments that led to (27) in

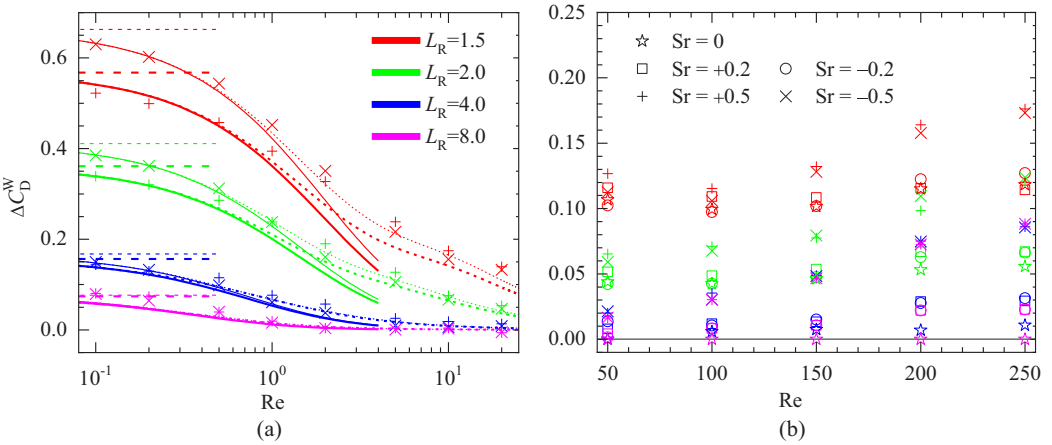

FIG. 13. Relative near-wall drag increase ΔC_D^W for a nonrotating sphere translating parallel to a wall in a linear shear flow. (a) Low-to-moderate Reynolds number regime for $Sr = \pm 0.5$; (b) moderate-to-high Reynolds number regime for $Sr = \pm 0.2$ and ± 0.5. Symbols in (a): numerical results for $Sr = 0.5$ (+) and $Sr = -0.5$ (×). Dashed lines: asymptotic prediction (19) corresponding to conditions $L_u \ll 1$, $L_\omega \ll 1$; solid lines: low-but-finite-Re semiempirical expression (23); dotted lines: low-to-moderate-Re semiempirical expression (31). Thick (thin) lines correspond to positive (negative) Sr.

the unsheared case. The empirical counterpart of (27) is thus

$$\Delta C_D^W[\mathrm{Re} \lesssim 10] \approx f'_D(L_u)[a^W(\mathrm{Re}, L_R)]^2 \Delta C_D^{W\text{-in}}(L_R, \mathrm{Sr}), \tag{31}$$

with $\Delta C_D^{W\text{-in}}(L_R, \mathrm{Sr})$, $f'_D(L_u)$, and $a^W(\mathrm{Re}, L_R)$ as given in (18), (19), and (26), respectively. The dotted lines in Fig. 13 confirm that the corresponding predictions properly reproduce the variations of the numerical data up to $\mathrm{Re} \approx 10$.

Figure 13(b) displays the wall-induced drag force computed for $\mathrm{Re} \geqslant 50$. While the drag still decreases with the Reynolds number up to $\mathrm{Re} = 100$, a systematic increase is observed at higher Re whatever the distance to the wall. Moreover, in the same high-Re regime, drag variations are found to be virtually independent of the sign of Sr. However, for $\mathrm{Sr} = O(1)$, the magnitude of the shear, i.e., the norm of Sr, has a significant influence on the drag, with, for instance, a 45% increase of ΔC_D^W at $\mathrm{Re} = 250$ from $\mathrm{Sr} = \pm 0.2$ to ± 0.5. To better analyze these results, it is appropriate to consider the unbounded configuration first, in order to examine the relative drag change $\Delta C_{D\omega}^U(\mathrm{Re}, \mathrm{Sr}) = (C_{D\omega}^U(\mathrm{Re}, \mathrm{Sr}) - C_{D0}^U(\mathrm{Re}))/C_{D0}^U(\mathrm{Re})$ due solely to the influence of the ambient shear. Figure 14 shows how $\Delta C_{D\omega}^U(\mathrm{Re}, \mathrm{Sr})$ varies with both the Reynolds number and the dimensionless shear rate. An obvious symmetry argument indicates that $\Delta C_{D\omega}^U(\mathrm{Re}, \mathrm{Sr})$ cannot depend on the sign of Sr, a constraint confirmed by numerical results. To magnify the shear-induced drag variations, specific runs were carried out for $\mathrm{Sr} = 1$. While only marginal for $|\mathrm{Sr}| = 0.2$, the relative shear-induced drag increase is found to reach approximately 20% at $\mathrm{Re} = 250$ with $|\mathrm{Sr}| = 1$. Within the considered ranges of Sr and Re, $\Delta C_{D\omega}^U$ depends almost linearly on Sr and Re beyond $\mathrm{Re} \approx 150$, in agreement with the tendency observed in [9]. Fitting the results obtained at $\mathrm{Re} = 250$ yields

$$\Delta C_{D\omega}^U[\mathrm{Re} = O(100)] \approx 7.5 \times 10^{-4} |\mathrm{Sr}| \mathrm{Re}, \tag{32}$$

an estimate seen to properly capture the dominant trend revealed by numerical results for $\mathrm{Re} \gtrsim 200$, although it overestimates the drag increase at lower Reynolds numbers. A quantitative comparison with the findings reported in [9] reveals that present values for $\Delta C_{D\omega}^U$ are typically twice as large. We investigated the possible origin of such a large difference, suspecting in particular that results may be contaminated by artificial confinement effects induced by the outer boundary of

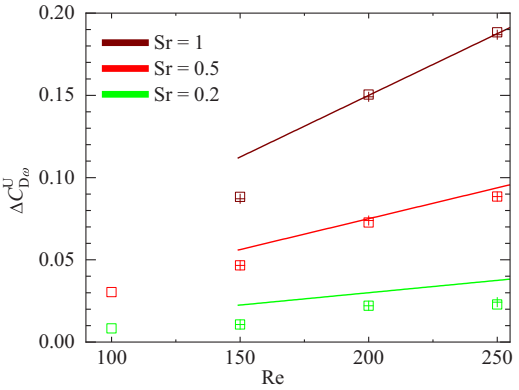

FIG. 14. Relative drag variation $\Delta C_{D\omega}^{U}$ on a sphere translating at moderate-to-high Reynolds number in an unbounded shear flow, with respect to the drag in a uniform stream. Symbols: numerical results for $\mathrm{Sr} > 0$ (□), and $\mathrm{Sr} < 0$ (+); lines: prediction of (32).

the computational domain, especially in the wake region. To check this possibility, we reran the simulations corresponding to $\mathrm{Re} = 200$ on a domain twice as large as the standard one, i.e., with the outer boundary located $40d$ from the sphere center, the radial resolution being kept unchanged close to the sphere, especially within the boundary layer, by increasing the number of nodes. The drag was found to vary by less than 0.3% in all cases, inducing variations of $\Delta C_{D\omega}^{U}$ not exceeding 2%. These tests make us confident that present results for the high-Re shear-induced drag increase are robust, being especially almost independent of the position of the domain outer boundary. In contrast, we suspect that this issue may have affected the results reported in [9], as that study made use of an ellipsoidal grid extending only to $10d$ upstream and downstream of the sphere and $5d$ in the direction perpendicular to the incoming flow.

Coming back to the near-wall situation, we first evaluated how the observed drag variation, ΔC_{D}^{W}, compares with the sum of the slip effect in the shearless case, ΔC_{Du}^{W}, and the shear effect in the unbounded configuration, $\Delta C_{D\omega}^{U}$, as given by (28) and (32), respectively. It turned out that this sum consistently overestimates ΔC_{D}^{W}, and the shorter the wall-particle separation the larger the overestimate. This finding implies that the shear-induced drag correction observed in the unbounded case is actually reduced by the presence of the wall, owing to the modifications the latter imposes on the wake structure. Keeping Re and Sr fixed and varying L_R, we observed that the excess quantity $\Delta C_{Du}^{W} + \Delta C_{D\omega}^{U} - \Delta C_{D}^{W}$ varies as the inverse of the separation. Introducing the shear-induced drag modification in the presence of the wall, $\Delta C_{D\omega}^{W}$, such that $\Delta C_{D}^{W} = \Delta C_{Du}^{W} + \Delta C_{D\omega}^{W}$, and fitting the numerical data yields

$$\Delta C_{D\omega}^{W}[\mathrm{Re} = O(100)] \approx \left(1 - 0.54 L_R^{-1}\right) \Delta C_{D\omega}^{U}[\mathrm{Re} = O(100)], \tag{33}$$

with $\Delta C_{D\omega}^{U}[\mathrm{Re} = O(100)]$ as given by (32).

The relative difference between the observed drag variation ΔC_{D}^{W} and the prediction corresponding to the sum of (28) and (33) is shown in Fig. 15 for $\mathrm{Sr} = \pm 0.5$. It is seen that, beyond $\mathrm{Re} \approx 100$, this difference never exceeds 7%, confirming that the above empirical model properly captures the near-wall drag variations in the high-Re regime. Numerical results obtained throughout the range $0.1 \leqslant \mathrm{Re} \leqslant 250$, together with the corresponding predictions based on the semiempirical expressions established above, are displayed in Fig. 16. In a way similar to (29), a purely empirical expression combining linearly the models previously established in the low-to-moderate Reynolds number regime [Eq. (31)] and the high-Reynolds number regime [Eqs. (28), (32), and (33)] may be designed to improve the estimate of the drag increase in the intermediate range $10 \leqslant \mathrm{Re} \leqslant 100$. As

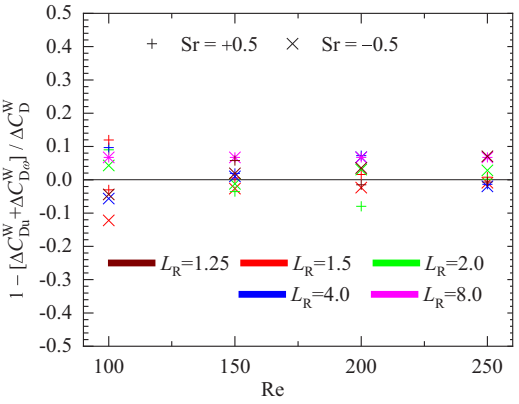

FIG. 15. Comparison for Sr = ±0.5 of the measured near-wall drag increase ΔC_D^W in the high-Reynolds-number regime with the prediction $\Delta C_{Du}^W[\mathrm{Re} = O(100)] + \Delta C_{D\omega}^W[\mathrm{Re} = O(100)]$ provided by the empirical models (28) and (33).

the dotted lines in Fig. 16 show, the composite expression

$$\Delta C_D^W \approx \Delta C_D^W[\mathrm{Re} = O(1-10)] + c_{D\omega\infty}\left\{\Delta C_{Du}^W[\mathrm{Re} = O(100)] + \Delta C_{D\omega}^W[\mathrm{Re} = O(100)]\right\} \quad \text{with}$$

$$c_{D\omega\infty} = 1 - e^{-0.035\mathrm{Re}^{0.75}} \tag{34a,b}$$

correctly fits the numerical data throughout the entire range of Reynolds number. Note that some data from [17,29] (the former for Sr = 0.25) and [30] are also included in Fig. 16 for comparison. Since the reference drag coefficient C_{D0}^U is not provided in these works, we again used the procedure described in Sec. V A 1 to determine ΔC_D^W. The low-Re data from [29] for Re = 0.2 stand slightly below present predictions. In contrast, those extracted from [17] and [30] stand somewhat above

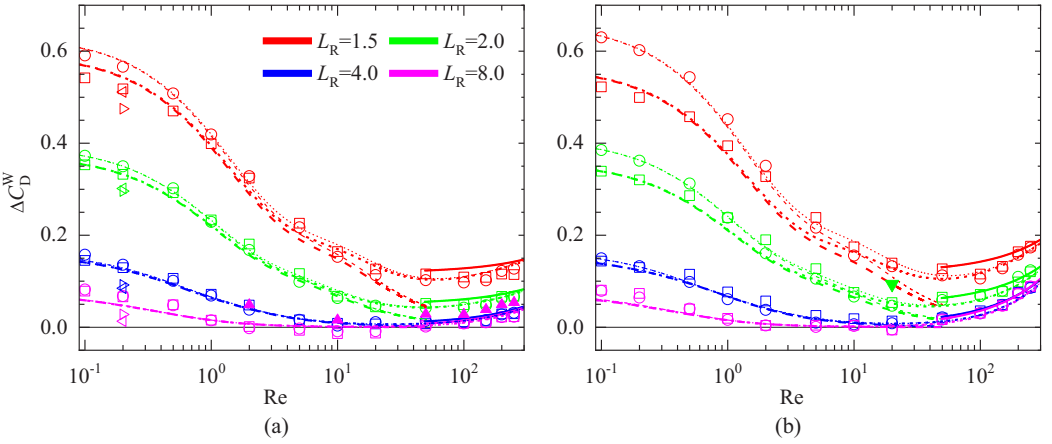

FIG. 16. Relative near-wall drag increase $\Delta C_D^W(\mathrm{Re}, \mathrm{Sr}, L_R)$ for a nonrotating sphere translating parallel to a wall in a linear shear flow, throughout the Re range investigated numerically. (a) Sr = ±0.2; (b) Sr = ±0.5. □ and ○: present numerical data for Sr > 0 and Sr < 0, respectively; ◁ and ▷: numerical data from [29] for Sr = −0.2 and Sr = +0.2, respectively; ▲: numerical data from [17] for Sr = 0.25; ▼: numerical data from [30] for Sr = +0.5. Thick solid lines: high-Re model based on the sum of (28) and (33); thick (thin) dashed lines: low-to-moderate-Re expression (31) for positive (negative) Sr; thick (thin) dotted lines: composite fit (34) for positive (negative) Sr.

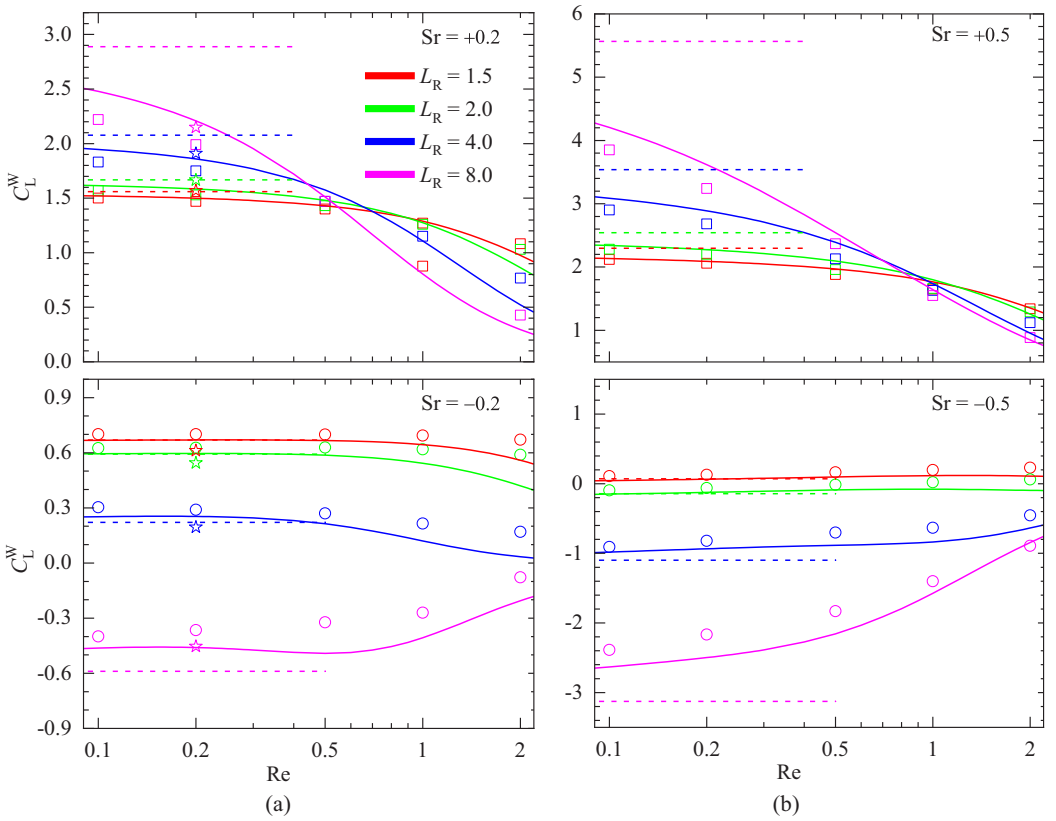

FIG. 17. Variations of the lift coefficient $C_L^W(\mathrm{Re}, \mathrm{Sr}, L_R)$ for a nonrotating sphere translating parallel to a wall in a linear shear flow at $\mathrm{Re} \leqslant 2$. (a) $\mathrm{Sr} = \pm 0.2$; (b) $\mathrm{Sr} = \pm 0.5$. □ and ○: numerical data for $\mathrm{Sr} > 0$ and $\mathrm{Sr} < 0$, respectively; ☆: numerical data from [29] for a freely rotating sphere (values for $L_R = 1.5$ with $\mathrm{Sr} = \pm 0.2$ and $L_R = 8$ with $\mathrm{Sr} = -0.2$ were interpolated from neighboring separations). Dashed lines: inner solution (15) corresponding to conditions $L_u \ll 1$, $L_\omega \ll 1$; solid lines: finite-Re expression (21) with f_L and h_L as given by (22a) and (22b), respectively.

them. These differences contrast with the close agreement observed in Fig. 10 in the case of a fluid at rest. The uncertainty introduced by the indirect procedure used to compute ΔC_D^W is presumably responsible for the most part of the observed differences. The slightly larger Sr in the series extracted from [17] also contributes to increase the corresponding ΔC_D^W compared to present results.

2. Lift on a nonrotating sphere

Figure 17 shows the computed lift coefficient $C_L^W(\mathrm{Re}, \mathrm{Sr}, L_R)$ up to $\mathrm{Re} = 2$ for various normalized shear rates and separation distances. Variations of C_L^W with increasing Re and L_R, as well as the form of the interplay between the shear- and slip-induced contributions, are consistent with those observed with clean spherical bubbles in [31]. For this reason, the reader is referred to Sec. 6.2.2 of that reference for a discussion of the physical mechanisms governing the variations of the lift force with Re, Sr and L_R revealed by Fig. 17. The reason why the lift force acting on a rigid sphere or a clean spherical bubble behave similarly in this regime has been established in [47] and extended to near-wall configurations in [22,48]. Specifically, these analyses indicate that, to leading order, shear-, wall-, and the combined lift forces acting on a rigid sphere in the low-but-finite Reynolds number regime differ from those on a clean spherical bubble only by a prefactor of $(3/2)^2$, $3/2$ being

the strength ratio of the respective Stokeslets. That the lift force on a rigid sphere at a given Sr and L_R is larger than that on a clean bubble by a factor of $(3/2)^2 = 2.25$ may be confirmed by comparing present data at Re = 0.1 with their counterparts in Fig. 18 of [31]. As expected, the dashed lines in Fig. 17 indicate that the asymptotic expression (15) corresponding to situations in which the wall stands in the inner region of the disturbance predicts the computed lift force well for small enough L_R and Re, typically $L_R < 4$ and $\mathrm{Re} \leqslant 0.2$ for both shear rates. When L_R or Re increases, the wall shifts to the outer region of the disturbance, and it is no surprise that (15) fails to capture the variations of the lift coefficient [e.g., with Re = 0.1 and $L_R = 8$, for which L_u and L_ω are both of $O(1)$]. In contrast, expression (21) [along with (22a) and (22b) for f_L and h_L, respectively] (solid lines in Fig. 17) properly accounts for finite-L_ω and finite-L_u effects, as it approximates C_L^W with a 10% accuracy at Re = 0.1 whatever L_R and Sr. As Re increases, the magnitude of the lift force decreases, owing to the decrease of the slip-induced contribution. Expression (21) properly captures this trend for both positive and negative Sr. Predictions remain accurate up to Re = 2 for $\mathrm{Sr} = \pm 0.5$ but deteriorate somewhat beyond $\mathrm{Re} \approx 0.5$ for $\mathrm{Sr} = \pm 0.2$. The reason for this is readily understood by noting that, under such low-shear conditions, ε ranges from 0.6 for Re = 0.5 down to 0.3 for Re = 2. For such modest shear levels, the theoretical solution of [19] is known to have a limited accuracy, as does that of [6] for $\varepsilon \lesssim 0.8$ in the unbounded case (see, for instance, the discussion in [29,35]). Since the fitting functions f_L and h_L were designed to approach this theoretical solution, it is no surprise that the accuracy of predictions based on the overall fit (21) involving these functions deteriorates as ε decreases.

In Fig. 17 we also reported numerical data from [29] for $\mathrm{Sr} = \pm 0.2$ and Re = 0.2 (the highest Reynolds number considered in this reference). As no data for a nonrotating sphere in a wall-bounded shear flow were provided, these data correspond to a freely rotating sphere. Hence, the expected effect of the particle rotation has to be subtracted to achieve a proper comparison with present results. In the limit of large separations, the discussion in Sec. III B indicates that the rotation adds a contribution $\frac{1}{2}\mathrm{Sr} - \frac{1}{32}\mathrm{Sr}^2$ to the lift coefficient. Based on this estimate, one expects the absolute values of C_L^W provided in [29] to exceed those obtained in the present study by a difference close to 0.1 for $|\mathrm{Sr}| = 0.2$ and $L_R = 8$, which Fig. 17 confirms. More precisely, the difference between these corrected data and present results is less than 3% for both positive and negative Sr.

Figure 18 summarizes the behavior of $C_L^W(\mathrm{Re}, \mathrm{Sr}, L_R)$ for $0.1 \leqslant \mathrm{Re} \leqslant 150$ at various normalized shear rates and separation distances. Some data from [17] (at Sr = 0.25) and [30] are also included and show very good agreement with present predictions. The lift force is seen to vary sharply with both the Reynolds number and the separation distance for $\mathrm{Re} \lesssim 10$, while at higher Reynolds number substantial variations only subsist for $L_R \lesssim 2$. For larger separations, the magnitude of the lift force gets close to that found in an unbounded flow (black solid lines in Fig. 18). Indeed, at such Reynolds numbers the thickness of the boundary layer around the sphere is small enough for the vortical interaction with the wall to have only a secondary influence on the lift force (see Fig. 3). Effects caused by the shear may be qualitatively estimated by comparing $C_L^W(\mathrm{Re}, \mathrm{Sr}, L_R)$ with its counterpart in the shearless situation, $C_{Lu}^W(\mathrm{Re}, L_R)$, shown in Fig. 18 for $L_R = 1.5$ (red solid lines). Clearly, the slip effect dominates for $\mathrm{Re} \gtrsim 10$. Influence of the shear becomes more pronounced or even dominant at lower Reynolds numbers. For large separations, it increases (decreases) the total lift force well beyond (below) the level reached in the shearless case for $\mathrm{Sr} > 0$ ($\mathrm{Sr} < 0$). The influence of Sr weakens as L_R decreases, the presence of the wall inhibiting the development of the wake. Selecting for instance $L_R = 1.5$, Re = 1, and Sr = 0.5, the difference between C_L^W and C_{Lu}^W is 0.66, three times less than the lift coefficient $C_{L\omega}^U = 1.93$ in the unbounded case. Based on the above observations, and disregarding the small shear-induced contribution to the lift beyond $\mathrm{Re} \approx 10$, the finite-Re expression (21) may be extended to moderate Reynolds numbers in the form

$$C_L^W[\mathrm{Re} = O(1-100)] \approx g_L C_{Lu}^W[\mathrm{Re} = O(1-100)] + h_L C_{L\omega}^U(\mathrm{Re} \ll 1), \tag{35}$$

$$\text{with} \quad g_L(L_\omega, \varepsilon, \mathrm{Re}) = e^{-0.22\varepsilon^{0.8} L_\omega^{2.5} \exp(-0.01\mathrm{Re}^2)}, \tag{36}$$

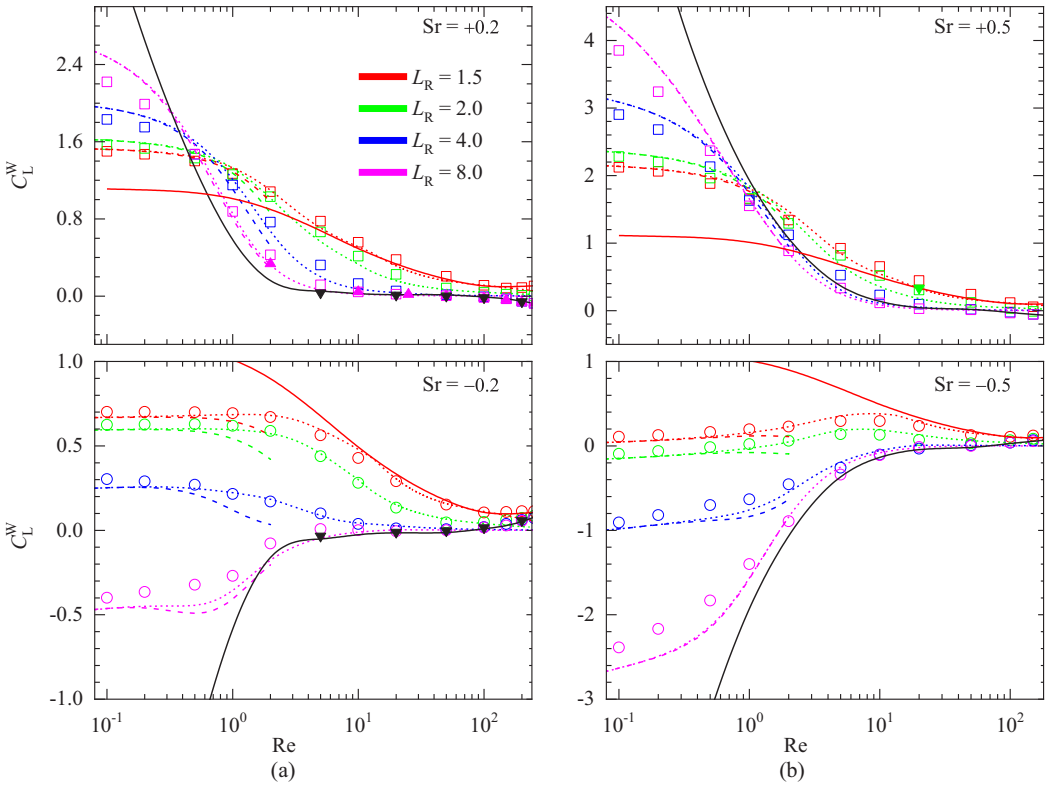

FIG. 18. Lift coefficient $C_L^W(\mathrm{Re}, \mathrm{Sr}, L_R)$ for a nonrotating sphere translating parallel to a wall in a linear shear flow at $\mathrm{Re} \leqslant 150$. (a) $\mathrm{Sr} = \pm 0.2$; (b) $\mathrm{Sr} = \pm 0.5$. □ and ○: numerical data for $\mathrm{Sr} > 0$ and $\mathrm{Sr} < 0$, respectively. ▲: numerical data from [17] for $\mathrm{Sr} = 0.25$; ▼: numerical data from [30]; ▼ data from [11] in the unbounded configuration. Dashed lines: finite-Re prediction (21); dotted lines: prediction (35); black solid lines: lift coefficient $C_{L\omega}^U$ in an unbounded shear flow (fitted from the results obtained with the present code); red solid lines: lift coefficient C_{Lu}^W at $L_R = 1.5$ in a wall-bounded fluid at rest.

and $C_{Lu}^W[\mathrm{Re} = O(1 - 100)]$, h_L and $C_{L\omega}^U(\mathrm{Re} \ll 1)$ as provided by (24), (22b), and (7), respectively. Note that, similar to expressions (21) and (22a) in the low-but-finite Reynolds number regime, (35) and (36) indicate that the wall and shear effects do not superimpose linearly, as the prefactor g_L for the former involves Sr through the presence of ε and L_ω. As shown in Fig. 18, (35) fits all numerical predictions well throughout the range $0.1 \leqslant \mathrm{Re} \leqslant 100$ for $L_R \leqslant 8$, with, however, a slight underestimation of the lift force in the range $5 \lesssim \mathrm{Re} \lesssim 50$ for positive Sr.

We now turn to the high-Reynolds-number regime, say, $\mathrm{Re} \gtrsim 100$. At such Reynolds numbers, the shear-induced lift force observed in the unbounded case has changed sign, as illustrated in Fig. 6. This is confirmed in Fig. 19 , the top left panel of which shows in passing that present predictions for the negative shear-induced lift force obtained with $\mathrm{Sr} = 0.2$ and 0.5 in the limit $L_R \to \infty$ (actually $L_R = 40$) compare well with numerical data from [9] and [11]. For small separations, typically $L_R \lesssim 2$, the slip-induced transverse force discussed in Sec. V A 2 remains non-negligible up to $\mathrm{Re} = 200$. When the two effects combine, the streamwise vorticity distribution illustrated in Fig. 4 suggests that the two mechanisms act in an antagonistic (cooperative) manner when Sr is positive (negative). This is confirmed in Fig. 19, where, taking the results corresponding to $\mathrm{Sr} = 0$ (black line) as reference, a negative Sr is seen to contribute positively to the lift force and *vice versa*, unlike the low-to-moderate Reynolds number phenomenology. Moreover, slip- and shear-induced effects combine in a strongly nonlinear manner. Indeed, for a given magnitude of Sr and a decreasing L_R,

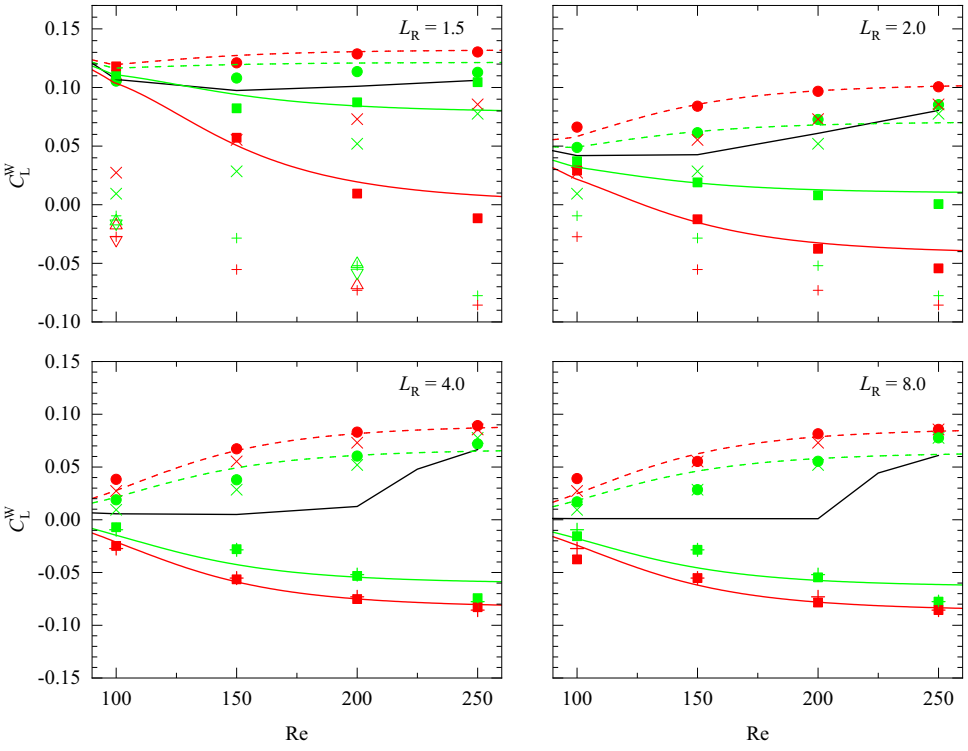

FIG. 19. Variations of the lift coefficient $C_L^W(\mathrm{Re}, \mathrm{Sr}, L_R)$ in the range $100 \leqslant \mathrm{Re} \leqslant 250$ for a nonrotating sphere translating parallel to a wall in a linear shear flow. ■ : $\mathrm{Sr} = +0.2$, ● : $\mathrm{Sr} = -0.2$, ■ : $\mathrm{Sr} = +0.5$, ● : $\mathrm{Sr} = -0.5$. Unbounded shear flow: + and + (all panels): $\mathrm{Sr} = +0.5$ and $+0.2$, respectively; same with × and × for $\mathrm{Sr} = -0.5$ and -0.2, respectively; △ and △ (top left panel): data from [9] for $\mathrm{Sr} = +0.5$ (interpolated) and $\mathrm{Sr} = +0.2$, respectively; ▽ and ▽ (top left panel): data from [11] for $\mathrm{Sr} = +0.4$ and $\mathrm{Sr} = +0.2$, respectively. Black solid line: $\mathrm{Sr} = 0$; green solid (dashed) line: prediction (37) for $\mathrm{Sr} = +0.2$ (-0.2); same with the red solid (dashed) line for $\mathrm{Sr} = +0.5$ (-0.5).

the shear-induced variation, $|C_L^W - C_{Lu}^W|$, is seen to become significantly larger when Sr is positive (compare in particular the data pairs corresponding to $\mathrm{Sr} = \pm 0.5$ at $L_R = 1.5$). For $\mathrm{Re} \gtrsim 200$ and $\mathrm{Sr} = 0$, the stationary imperfect bifurcation discussed in Sec. IV A takes place when the separation is large enough, causing a sharp increase in the transverse force, as the black lines in Fig. 19 confirm for $L_R \geqslant 4$. For smaller separations, or for arbitrary separations in the presence of shear, no bifurcation takes place in this Re range, since the flow past the sphere is fully three-dimensional whatever Re. This is the reason why the increase in the magnitude of C_L^W with Re is much more gradual in such situations. As the comparison with data corresponding to the unbounded sheared configuration (crosses) reveals, the wall no longer influences the lift force for $L_R \gtrsim 4$. Conversely, for smaller separations, the lift force found for $\mathrm{Sr} > 0$ $(\mathrm{Sr} < 0)$ reduces (increases) gradually compared to its value in an unbounded flow as L_R decreases. We sought a correlation capable of reproducing the above trends. For this purpose, since the shear-induced lift in an unbounded flow changes sign for $\mathrm{Re} \approx 50$, we used the expression provided in (11) for $C_{L\omega}^U[\mathrm{Re} = O(100)]$. Then Fig. 12(b) suggests that the slip-induced contribution C_{Lu}^W is almost constant beyond $\mathrm{Re} = 100$ when no stationary bifurcation takes place (see the data set corresponding to $L_R = 1.5$). This situation also holds when $\mathrm{Sr} \neq 0$, since the wake is three-dimensional whatever Re, similar to the configuration $\mathrm{Sr} = 0$ when L_R is small. Therefore it sounds reasonable to assume that, at a given separation, $C_{Lu}^W(\mathrm{Sr} \neq 0, \mathrm{Re} \geqslant 100)$ is close to $C_{Lu}^W(\mathrm{Re} = 100)$ for $\mathrm{Sr} = 0$, as provided by (24) for $\mathrm{Re} = 100$.

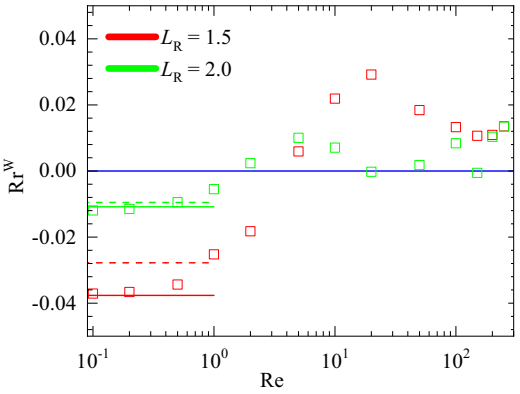

FIG. 20. Variations with Re and L_R of the rotation rate Rr^W of a torque-free sphere translating parallel to a wall in a fluid at rest. Symbols: numerical results; dashed lines: asymptotic prediction (17) corresponding to the condition $L_u \ll 1$; solid lines: empirical extension (39) of (17) based on the exact zero-Re prediction of [38,49].

Last, $C_{L\omega}^U[\mathrm{Re} = O(100)]$ has to be weighted by a prefactor $k_L(L_R, \mathrm{Re})$, in order to mimic the increasingly asymmetric magnitude of the lift force according to the sign of Sr when L_R becomes small. We finally obtained

$$C_L^W[\mathrm{Re} = O(100)] \approx C_{Lu}^W(\mathrm{Re} = 100) + k_L C_{L\omega}^U[\mathrm{Re} = O(100)], \tag{37}$$

$$\text{with} \quad k_L(L_R, \mathrm{Re}) = 1 - e^{-0.034 L_R^6 |\mathrm{Sr}|^{0.75}} + [1 + \mathrm{sgn}(\mathrm{Sr})] e^{-0.048 L_R^{4.5} |\mathrm{Sr}|^{-1}} e^{-(0.009\mathrm{Re})^{-4}}, \tag{38}$$

with $C_{Lu}^W(\mathrm{Re} = 100)$ and $C_{L\omega}^U[\mathrm{Re} = O(100)]$ as provided by (24) and (11), respectively. The solid and dashed lines in Fig. 19 confirm that this correlation properly captures the dramatic variations induced by the wall on the lift force, including the asymmetry observed between negative and positive relative shear rates.

3. Effects of sphere rotation

The rotation rate of a torque-free sphere translating parallel to the wall in a fluid at rest is shown in Fig. 20 for the shortest two separations, $L_R = 1.5$ and 2, over the range $0.1 \leqslant \mathrm{Re} \leqslant 250$. Rr^W is seen to change from negative at low Reynolds number (in agreement with Faxén's prediction (17) [43]) to positive beyond a critical $O(1)$ Reynolds number, Re_{c_T}. This critical value depends on L_R, and numerical results indicate $\mathrm{Re}_{c_T} \approx 4$ for $L_R = 1.5$ and $\mathrm{Re}_{c_T} \approx 2$ for $L_R = 2$. The low-Re numerical values are found to exceed those predicted by (17), especially for $L_R = 1.5$. We compared the exact creeping-flow values provided in [38] (recomputed from the exact solution of [49]) with Faxén's approximate prediction (17) and found that the latter significantly underestimates the former for $L_R \lesssim 2$. A significantly better approximation, reproducing the exact prediction down to $L_R \approx 1.1$, is provided by the semiempirical extension of (17)

$$\mathrm{Rr}^W(L_R, \mathrm{Re} \ll 1) \approx -\tfrac{3}{16} L_R^{-4} \left(1 - \tfrac{3}{8} L_R^{-1} + 0.9 L_R^{-3}\right), \tag{39}$$

suggesting that higher-order corrections neglected in Faxén's solution are required to accurately estimate Rr^W at such small separations. As the solid lines in Fig. 20 indicate, numerical results at $\mathrm{Re} = 0.1$ are in close agreement with (39). For $\mathrm{Re} > \mathrm{Re}_{c_T}$, the rotation rate first increases up to a maximum ($Rr^W \approx 0.01$ at $\mathrm{Re} \approx 5$ for $L_R = 2$, $Rr^W \approx 0.029$ at $\mathrm{Re} \approx 20$ for $L_R = 1.5$), before exhibiting non-monotonic variations with both the Reynolds number and the separation distance, especially beyond $\mathrm{Re} = 100$. A qualitatively similar behavior has been reported in [16] for the torque on a nonrotating sphere in the same range of separations. We hypothesize that subtle

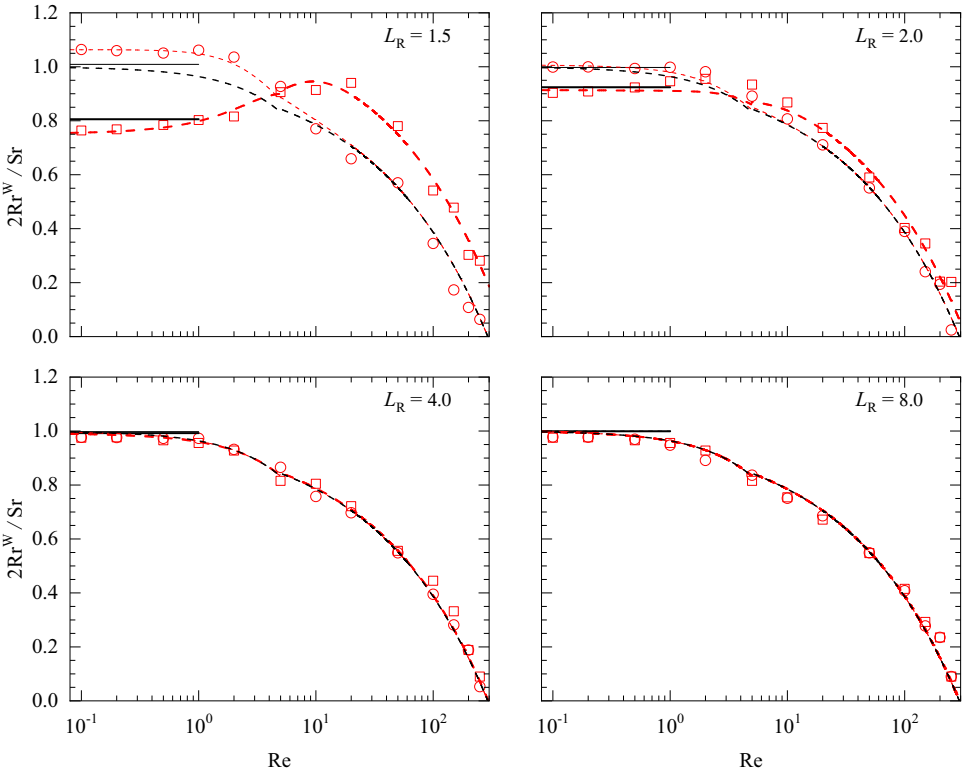

FIG. 21. Variations with Re and L_R of the normalized rotation rate $2Rr^W/Sr$ of a torque-free sphere translating parallel to a wall in a linear shear flow with $|Sr| = 0.5$. □ and ○: numerical data for $Sr > 0$ and $Sr < 0$, respectively. Solid lines: inner solution (17) corresponding to conditions $L_u \ll 1$, $L_\omega \ll 1$; black dashed lines: empirical prediction (13)-(14) from [11] in an unbounded shear flow; red dashed lines: empirical fit (40). Thick and thin lines refer to predictions for $Sr = +0.5$ and $Sr = -0.5$, respectively.

variations in the flow structure in the sphere vicinity (see Fig. 3 in [16]) are responsible for this complex behavior.

Figure 21 summarizes the normalized rotation rate $2Rr^W/Sr$ corresponding to the torque-free condition, as computed for $0.1 \leqslant Re \leqslant 250$ at various separation distances. Only the "strong" relative shear rate $|Sr| = 0.5$ is considered, so as to obtain sizable rotation effects. At low Reynolds numbers and small separations ($0.1 \leqslant Re \lesssim 5$, $L_R \leqslant 2$), numerical data indicate that spheres moving under $Sr < 0$ conditions rotate faster than those moving with $Sr > 0$. This difference is the consequence of the opposite signs of the shear- and slip-induced contributions to the sphere rotation in the low-Reynolds number regime, as is apparent in (17) (in the configuration of Fig. 1, these two contributions yield clockwise and counterclockwise rotations, respectively). This asymptotic prediction (solid lines in Fig. 21) is in good agreement with the numerical data up to $Re = 0.5$. A slight underestimate (overestimate) is noticed when $L_R = 1.5$ for $Sr < 0$ ($Sr > 0$), in line with the aforementioned underestimate of the slip effect by (17) at short separations. The influence of the sign of Sr on the magnitude of Rr^W is seen to reverse at somewhat higher Re, the rotation rate becoming larger for positive relative shear rates than for negative ones when the Reynolds number exceeds the critical value $Re \approx 6$ ($Re \approx 3$) for $L_R = 1.5$ ($L_R = 2$). This change is a direct consequence of the change of sign of the slip-induced rotation in a fluid at rest, as described above. Thus, when the sphere is allowed to rotate in the moderately inertial regime, the direction of the slip-induced rotation is opposite to that found in the low-Re regime, leading to a cooperative (antagonistic) effect with the

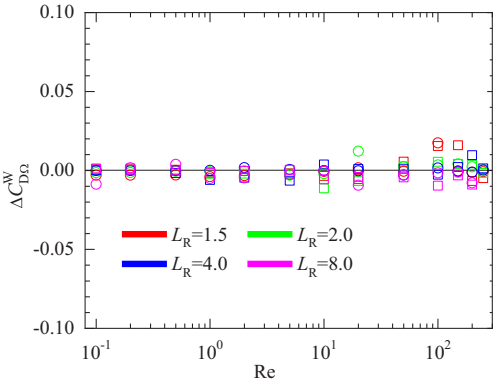

FIG. 22. Influence of the sphere rotation induced by the torque-free condition on the relative drag increase for $|\mathrm{Sr}| = 0.5$. Symbols □ and ○ refer to $\mathrm{Sr} = +0.5$ and $\mathrm{Sr} = -0.5$, respectively.

shear when Sr is positive (negative). Beyond $L_R = 2$, the normalized rotation rates obtained with positive and negative Sr are virtually identical, suggesting that the slip effect has become negligible at such separations compared to that of the shear. Comparing the two panels at $L_R = 4$ and $L_R = 8$ indicates that the shear effect itself is barely affected by the presence of the wall at such separations, the rotation rates found at a given Re being very close for both values of L_R. This conclusion is reinforced by the good agreement between present results for $L_R \geqslant 4$ and the fit (13)-(14) provided in [11] (black dashed lines in Fig. 21), which is based on numerical results obtained in an unbounded shear flow. Both sets of results show that the rotation rate gradually decreases as the Reynolds number increases, and is reduced to approximately 40% (20%) of the low-Re value $\mathrm{Rr} = \frac{1}{2}\mathrm{Sr}$ at $\mathrm{Re} = 100$ (200). Remarkably, results at the lowest two separations reveal that the rotation rate is altered by the presence of the wall in a very dissimilar manner depending on the sign of Sr in the moderate-to-large Reynolds number regime, say, $\mathrm{Re} \gtrsim 10$: while Rr^{W} is significantly larger than the rotation rate found in an unbounded shear flow when Sr is positive (even for $\mathrm{Re} \gtrsim 100$), the wall does not seem to have any significant effect for $\mathrm{Re} \geqslant 10$ when Sr is negative.

To account for these various effects, we sought an empirical fit tending toward (17) when $\mathrm{Re} \to 0$ [with the empirical modification introduced in (39)] and toward (13)–(14) when $L_R \to \infty$, while taking into account the aforementioned asymmetric sgn(Sr)-dependent influence of the wall at moderate-to-large Re. We found that the best fit satisfying these requirements is

$$\mathrm{Rr}^{W} \approx -\frac{3}{16} f_L' L_R^{-4} \left\{ 1 - \frac{3}{8} L_R^{-1} + 0.9 L_R^{-3} \right\} + \left\{ f_\Omega^{U} + 0.5 L_R^{-4} \tanh\left(\frac{\mathrm{Re}}{2}\right)[1 + \mathrm{sgn}(\mathrm{Sr})] \right\} \left\{ 1 - \frac{5}{16} L_R^{-3} e^{-0.5\mathrm{Re}} \right\} \frac{\mathrm{Sr}}{2}, \tag{40}$$

with f_L' and f_Ω^{U} as given in (20) and (14), respectively. As the dashed lines in Fig. 21 show, (40) satisfactorily matches the numerical data throughout the considered range of Re and L_R.

The difference $\Delta C_{D\Omega}^{W}$ between the relative drag variations ΔC_D^{W} respectively found in the torque-free and nonrotating near-wall configurations for a given set of $(\mathrm{Re}, \mathrm{Sr}, L_R)$ is shown in Fig. 22. Throughout the considered range of parameters, $\Delta C_{D\Omega}^{W}$ is less than 2%, indicating that the sphere rotation has only a marginal effect on the drag. Note that $\Delta C_{D\Omega}^{W}$ is even less than 1% for $\mathrm{Re} < 100$, the largest influence of the rotation being observed in the high-Reynolds-number regime. This weak change in the drag force confirms the findings of [16]. It is in line with the comments made in Sec. IV B regarding the tiny changes induced in the spanwise vorticity field by the sphere rotation resulting from the torque-free condition. At low Reynolds number, it is also in line with the

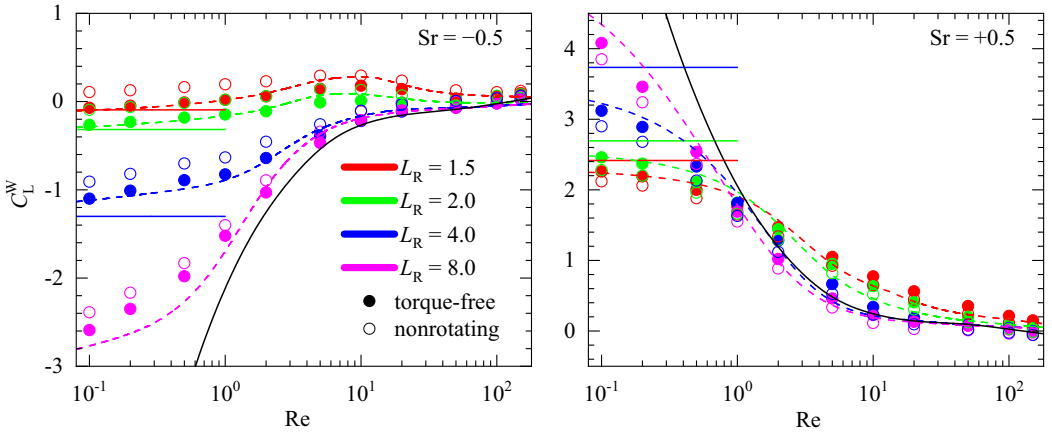

FIG. 23. Influence of the sphere rotation induced by the torque-free condition on the lift force for $|\mathrm{Sr}| = 0.5$ and $0.1 \leqslant \mathrm{Re} \leqslant 150$. Closed and open symbols refer to the lift coefficient for torque-free and nonrotating spheres, respectively. Horizontal solid lines: asymptotic prediction (16) corresponding to conditions $L_u \ll 1$, $L_\omega \ll 1$, $L_\Omega \ll 1$; dashed lines: empirical prediction (41); black solid line: total lift coefficient for a torque-free sphere in an unbounded shear flow (fitted from the results obtained with the present code).

theoretical predictions (17) and (18) which indicate that the drag force is affected by the particle rotation only at $O(L_R^{-8})$.

Things are somewhat different regarding the lift force. As seen in Fig. 23, the lift force in the torque-free case (closed symbols) slightly but consistently differs from its counterpart in the nonrotating case (open symbols) for large enough relative shear rates (here $|\mathrm{Sr}| = 0.5$). The rotation provides a positive contribution when the sphere lags the fluid ($\mathrm{Sr} > 0$) and *vice versa*. Whatever the sign of Sr, this effect reduces as Re increases, in a manner consistent with the variation of the torque-free rotation rate observed in Fig. 21. The asymptotic prediction (16) derived under conditions $L_u \ll 1$, $L_\omega \ll 1$, $L_\Omega \ll 1$ is in good agreement with the data obtained at $\mathrm{Re} = 0.1$ up to $L_R \approx 2$ for $\mathrm{Sr} > 0$, and $L_R \approx 4$ for $\mathrm{Sr} < 0$. That the range of accuracy of the asymptotic prediction is somewhat larger for negative relative shear rates is a property shared with the nonrotating case (compare the left and right panels in Fig. 17). This is presumably because the nonlinear interaction between the slip-induced and shear-induced mechanisms contributing to the lift force is somewhat weaker when the two mechanisms are antagonistic, i.e., when $\mathrm{Sr} < 0$.

To extend empirically the validity of (16) toward moderate Reynolds numbers, the change $C_{L\Omega}^W$ in the lift force specifically due to the torque-free rotation, which may be thought of as a Magnus lift component, must first be examined in detail. As Fig. 24 shows, when normalized by the rotation rate Rr^W, this change only weakly depends on Re, especially for small separations. A similar behavior was observed in [11] in an unbounded shear flow. The rough approximation $C_{L\Omega}^U/\mathrm{Rr} \approx 0.55$ provided in this reference is in reasonable agreement with present data beyond $O(1)$ Reynolds numbers, as the solid lines in Fig. 24 show (the difference is larger at low Re, as expected from the difference between (16) and (15) which predicts $C_{L\Omega}^U/\mathrm{Rr} \approx 1 - \frac{1}{8}\mathrm{Rr}$ for large separations). Based on this finding, one can expect the total lift force acting on a torque-free rotating sphere with $\mathrm{Re} \gtrsim 1$ to be correctly estimated by superposing linearly the force found in the nonrotating case as given by (35) and the spin-induced contribution discussed above. This superposition yields

$$C_L^W[\mathrm{Re} = O(1-100)] \approx g_L C_{Lu}^W[\mathrm{Re} = O(1-100)] + h_L C_{L\omega}^U(\mathrm{Re} \ll 1) + 0.55\mathrm{Rr}^W, \qquad (41)$$

with Rr^W as provided in (40). The dashed lines in Fig. 23 confirm that this linear superposition fits the numerical data well up to $\mathrm{Re} \approx 100$, even in the low-Reynolds-number range provided the separation is not "too" large.

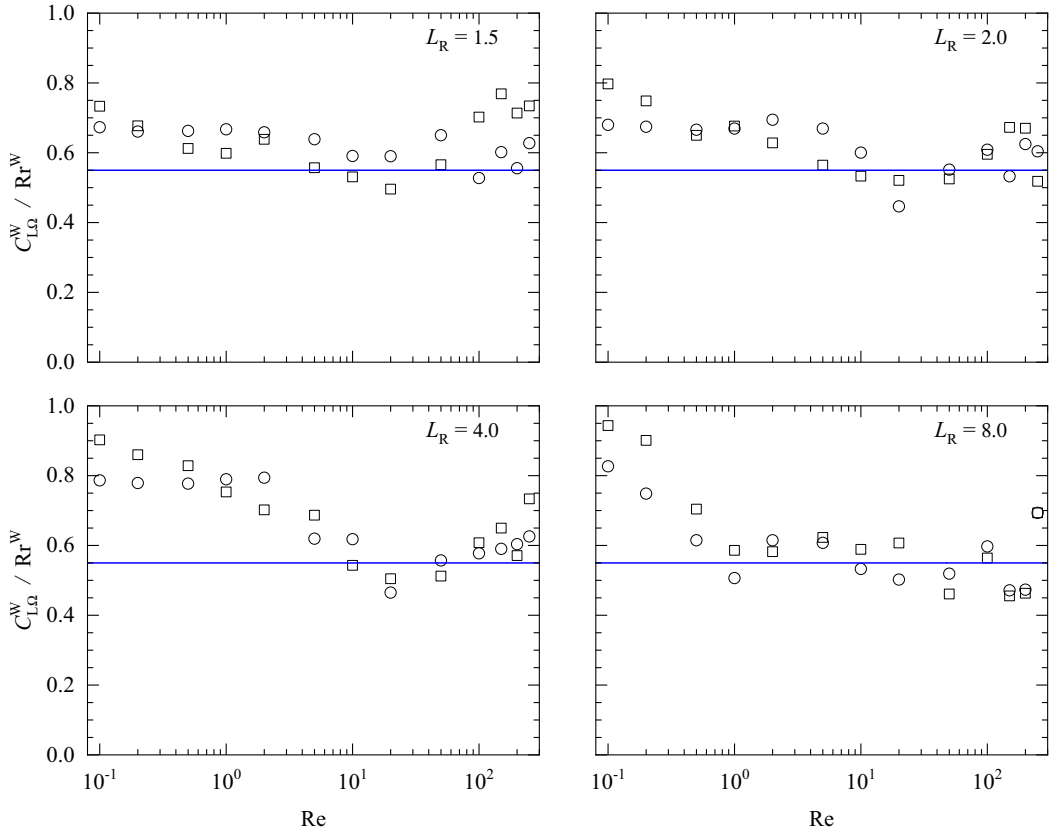

FIG. 24. Change in the lift coefficient due to the sphere rotation induced by the torque-free rotation. Values of $C^{W}_{L\Omega}$ are divided by the rotation rate Rr to provide a better collapse. □ and ○ symbols refer to numerical data for Sr $>$ 0 and Sr $<$ 0, respectively. Solid lines: approximation $C^{U}_{L\Omega}/\mathrm{Rr} \approx 0.55$ established in [11] in an unbounded shear flow.

In the high-Re regime Re $>$ 100, the total lift force is small, with lift coefficients typically of $O(0.1)$, i.e., one order of magnitude smaller than in the low-Re regime. However, the relative contribution of the change $C^{W}_{L\Omega}$ caused by the torque-free rotation in the total lift force remains significant, as Fig. 25 shows. Again, for a given Reynolds number and separation distance, $C^{W}_{L\Omega}$ is seen to be larger when Sr is positive, especially for $L_R \leqslant 2$. Moreover, the qualitative influence of the sphere rotation is found to depend crucially on the separation distance. Indeed, for Re $\geqslant$ 150, the torque-free condition is seen to decrease the magnitude of the total lift force irrespective of its sign for $L_R \geqslant 4$. This is no longer the case at the smallest two separations, for which lift forces corresponding to Sr $<$ 0 are still reduced by the rotation while those associated with positive Sr are enhanced, especially for $L_R = 1.5$. To approach the observed behaviors, we again considered that rotation-induced effects combine linearly with the slip- and shear-induced contributions predicted by (37), assuming that the empirical expression (40) for the rotation rate derived at moderate Reynolds number remains valid up to the upper bound (Re = 250) of the regime considered here. Figure 24 indicates that the ratio $C^{W}_{L\Omega}/\mathrm{Rr}^{W}$ is still close to 0.55 in this regime, although it seems to rise to slightly larger values (≈0.7) for positive Sr when the separation becomes small. Keeping this ratio unchanged, we obtain

$$C^{W}_{L}[\mathrm{Re} = O(100)] \approx C^{W}_{Lu}(\mathrm{Re} = 100) + k_L C^{U}_{L\omega}[\mathrm{Re} = O(100)] + 0.55\mathrm{Rr}^{W}. \tag{42}$$

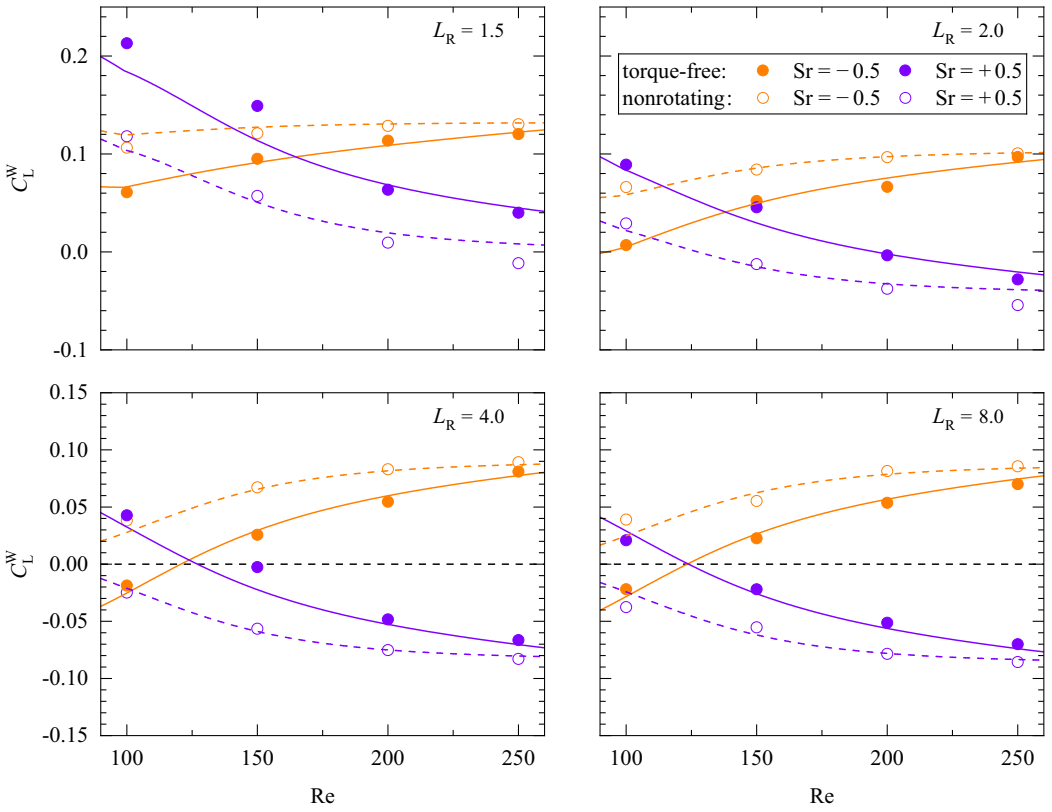

FIG. 25. Influence of the torque-free rotation on the lift force in the high-Reynolds-number regime for $|\mathrm{Sr}| = 0.5$. Closed and open symbols refer to data obtained with torque-free and nonrotating spheres, respectively. Solid and dashed lines correspond to the prediction of (42) for the torque-free and nonrotating cases, respectively. The horizontal black dashed line materializes the dividing line $C_L^W = 0$.

As Fig. 25 shows, this fit reproduces the observed trends well throughout the considered Reynolds number range, although the influence of the torque-free rotation appears to be slightly underestimated at small separations when Sr is positive. This successful extension of (37) indicates that effects of slip, shear and torque-free rotation may still be considered to contribute separately to the lift force even for $O(100)$ Reynolds numbers, provided of course the influence of the nearby wall is properly accounted for in the magnitude of each contribution.

An overview of the complex variations of the total lift force in the case of a torque-free particle is provided in Fig. 26. Numerical data discussed in Fig. 23 (and in Fig. 12 for the unsheared configuration) are replotted here against the separation-based Reynolds number $L_u = \frac{1}{2} L_R \mathrm{Re}$, providing a complementary view with respect to that offered by the previous plots. As expected, for $\mathrm{Sr} = 0$ [Fig. 26(b)], C_L is found to decay sharply as L_u increases, and to become vanishingly small for $L_u \gtrsim 10^2 - 10^3$ depending on Re, provided the Reynolds number is less than the threshold value $\mathrm{Re}^{SS} \approx 212$ at which the axisymmetric wake becomes unstable. This decay follows the L_u^{-2} prediction of (20) for $\mathrm{Re} \lesssim 1$ (solid black line) and sharpens as the Reynolds number further increases up to $\mathrm{Re} \approx \mathrm{Re}^{SS}$, as accounted for by (24). When the sphere lags behind the fluid [Fig. 26(c)], the slip- and shear-induced lift forces cooperate up to $\mathrm{Re} \approx 50$. As L_u increases, so does the shear-induced contribution, owing to the weakening of the wall-induced asymmetry imposed to the vorticity disturbance in the particle wake (see Sec. IV A). For $\mathrm{Re} \lesssim 1$, this increase in the shear-induced lift overtakes the decrease of the slip-induced contribution, making the overall force increase with

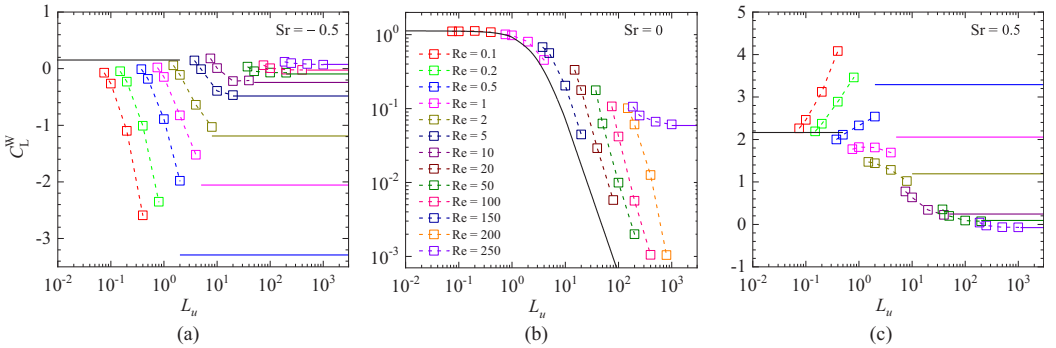

FIG. 26. Variations of the lift force vs the separation-based Reynolds number L_u for torque-free spheres translating at various Reynolds numbers in a wall-bounded flow. (a) $\mathrm{Sr} = -0.5$ (the sphere leads the fluid); (b) $\mathrm{Sr} = 0$ (the fluid is at rest at infinity); (c) $\mathrm{Sr} = +0.5$ (the sphere lags behind the fluid). Symbols: numerical results. Solid lines on the right part of each panel: asymptotic value of $\mathrm{C_L}$ in the unbounded configuration ($L_u \to \infty$); solid line on the left part of panels (a) and (c): asymptotic prediction (16) evaluated in the limit $L_\mathrm{R} \to 1$ (sphere touching the wall); black solid line in (b): prediction (20) from [14] valid for $\mathrm{Re} \ll 1$ and $L_u \gg 1$.

L_u. At moderate Reynolds number, the shear-induced lift force in the unbounded configuration is much smaller than in the low-Re regime. Because of this, the growth of this contribution as L_u increases can no longer compensate for the decrease of the slip-induced contribution, making the overall lift force decrease sharply with L_u as soon as $\mathrm{Re} \gtrsim 2$. The shear-induced lift changes sign for $\mathrm{Re} \gtrsim 50$, while the spin-induced lift does not. Hence, in the limit $L_u \gg 1$ and for larger Reynolds numbers, the sign of the total lift force depends on the relative magnitude of these two contributions. The former becoming dominant for $\mathrm{Re} \gtrsim 100$, the total force becomes negative at large enough Re and L_u, as illustrated by the purple series ($\mathrm{Re} = 250$). When the sphere leads the fluid [Fig. 26(a)] and the Reynolds number is low or moderate, the shear- and spin-induced lift contributions are both attractive, so that only the slip-induced contribution can make the overall lift force repulsive. This requires the separation to be small enough, as is the case in the range $1 \lesssim \mathrm{Re} \lesssim 50$ for the smallest L_u (according to Fig. 23, this would also be the case at lower Re in the case of a nonrotating particle). For the reasons reminded above, increasing L_u makes the slip-induced contribution decrease, while in this Reynolds number range it makes the magnitude of the shear-induced contribution increase. Therefore the overall lift force becomes negative beyond a (small) critical L_u and keeps on increasing in magnitude until it asymptotes the value it takes in the unbounded configuration at large enough L_u. Again, for $\mathrm{Re} \gtrsim 50$, the sign of the total lift force in the limit $L_u \gg 1$ depends on the relative magnitude of the shear- and spin-induced contributions. The latter is still slightly dominant for $\mathrm{Re} = 100$, yielding a tiny negative total lift force (pink series) but the former eventually takes over at larger Reynolds number, making the total force positive at $\mathrm{Re} = 250$ (purple series).

The above comments apply with only little changes to a nonrotating particle. Results in a fluid at rest are virtually identical (see Fig. 12). With $\mathrm{Sr} \neq 0$, the absence of the spin-induced contribution generally slightly decreases the magnitude of the total lift force. The only exceptions are the regimes in which this total force is very small, in which case this absence may change its sign. As pointed about above, this is the case for $\mathrm{Sr} < 0$ at low Reynolds number and $L_u \lesssim 10^{-1}$. For both negative and positive Sr, this is also the case at very large L_u in an intermediate, Sr-dependent range of Reynolds number just beyond the critical value at which the shear-induced lift changes sign. In this regime, the total lift force in the nonrotating case changes sign as soon as the shear-induced contribution does, i.e., for $\mathrm{Re} \approx 50$. In contrast, Fig. 26 shows that when the torque-free condition holds, the spin-induced contribution maintains the sign of the total force unchanged up to $\mathrm{Re} \approx 100$ for $|\mathrm{Sr}| = 0.5$.

VI. SUMMARY AND CONCLUDING REMARKS

We computed the flow and the hydrodynamic forces acting on a rigid sphere moving along the planar wall bounding a linear shear flow over a wide range of Reynolds number and separation distance, with the sphere either lagging or leading the fluid. We considered both nonrotating and torque-free spheres in order to quantify effects of the rotation induced by the torque-free constraint obeyed by freely moving particles. To reveal the slip-wall and shear-wall interaction mechanisms at stake, we examined several characteristic features of the flow field, especially the spatial distribution of the spanwise and streamwise vorticity disturbances, before focusing on their influence on the drag and lift forces.

When the sphere moves in a fluid at rest, low-Reynolds-number asymptotic solutions indicate an increase of the drag due to the presence of the wall. Additionally, a repulsive transverse force arises, due to the interaction between the wall and the wake resulting from the vorticity generated at the sphere surface by the no-slip condition. For a given separation distance, the magnitude of this repulsive force decreases with the Reynolds number when the wall lies in the outer region of the disturbance, in line with the conclusions of previous studies. At low-but-finite Reynolds number, both the drag increase and the transverse force are proportional to the square of the maximum vorticity at the sphere surface, which increases with the Reynolds number. Present results confirm these predictions, and support the model (24) proposed in [15] for the transverse force up to $O(100)$ Reynolds numbers, albeit with a slight change in the evaluation of the surface vorticity aimed at accounting for the influence of the nearby wall. At larger Reynolds number, the behavior of the transverse force depends crucially on the separation. For $L_R \geqslant 4$, this force is nearly zero from Reynolds numbers of some tens up to the critical value $\mathrm{Re}^{SS} \approx 212$ corresponding to the onset of a stationary nonaxisymmetric wake. Although the wall is not responsible for this change in the wake structure, it selects the direction of the corresponding lift force, which again tends to repel the sphere into the fluid for $\mathrm{Re} > \mathrm{Re}^{SS}$. Up to $\mathrm{Re} = 250$, the magnitude of this force is accurately estimated by the heuristic extension (30) of the theoretical prediction derived from a weakly nonlinear analysis. For smaller separations, the flow past the sphere remains anisotropic whatever the Reynolds number, making the transverse force keep significant values throughout the Re range explored numerically. In this situation, the force does not change much beyond $\mathrm{Re} = 100$ when the separation is small ($L_R = 1.5$), while a mixed situation in which the force increases significantly with the Reynolds number in the range $150 \lesssim \mathrm{Re} \lesssim 250$ takes place at intermediate separations ($L_R = 2$). At low Reynolds number, asymptotic predictions with the wall standing in the inner region of the disturbance predict that the shear tends to decrease (increase) the drag when the sphere lags (leads) the fluid, while the reverse holds for the transverse force. For this reason, the latter may switch from positive to negative at a given separation if the sphere leads the fluid and the relative magnitude of the shear is large enough. These predictions are confirmed, both qualitatively and quantitatively, by present numerical results. When the wall stands in the outer region of the disturbance, the semiempirical expressions of [31] taking into account finite-size effects are found to provide reliable predictions for both the drag variation and the lift force irrespective of the wall position up to $\mathrm{Re} = 2$. Whatever Sr and L_R, the magnitude of the lift force sharply decreases as the Reynolds number increases in the range $1 \lesssim \mathrm{Re} \lesssim 10$. For $L_R \gtrsim 2$, only a weak lift force, with a magnitude close to that found in an unbounded flow, subsists in the moderate-to-high Reynolds number regime $10 \lesssim \mathrm{Re} \lesssim 100$. This force keeps significantly larger values at smaller separations, being dominated by the slip effect rather than the influence of the shear in this Re range. Numerical results allowed us to obtain the empirical prediction (35)-(36) for the lift force extending the finite-Re prediction (21) up to $\mathrm{Re} \lesssim 100$.

At $O(100)$ Reynolds numbers, considering the unbounded sheared configuration first was found useful to quantify specific effects induced by the wall. Present results confirm the well-established reversal of the shear-induced lift beyond $\mathrm{Re} \approx 50$ [9]. Variations of this "reversed" lift force with Re and Sr agree well with those reported in the literature, as summarized in [36]. In the same regime, the drag force is found to increase linearly with Re and |Sr| beyond $\mathrm{Re} \approx 150$, leading to a

substantial increase ($\approx 20\%$) at $\mathrm{Re} = 250$ for $|\mathrm{Sr}| = 1$. When a nearby wall is involved, the above reversal makes the slip- and shear-related mechanisms contributing to the lift act in an antagonistic (cooperative) manner for positive (negative) Sr, unlike the situation encountered at lower Reynolds numbers. Moreover, these mechanisms interact in a highly nonlinear manner, the shear-induced variation to the lift force observed for a given magnitude of the relative shear rate being significantly larger when Sr is positive. We could summarize the effect of these complex interactions into the empirical prediction (37)-(38) which provides an accurate estimate of the near-wall lift force up to $\mathrm{Re} = 250$.

Only small changes are observed in the flow structure when the sphere rotates in order to satisfy a torque-free condition. The corresponding rotation rate decreases drastically as Re increases, similar to the tendency already reported in an unbounded shear flow. However, these small changes subtly modify the shear stress distribution at the sphere surface, hence the torque acting on it. For this reason, they are sufficient to make the variations of the rotation rate with respect to Re and Sr nontrivial in near-wall configurations. First, the slip-induced rotation in a fluid at rest is found to change sign beyond a critical separation-dependent $O(1)$ Reynolds number. Then, for small enough separations and Reynolds numbers $\gtrsim 10$, the rotation rate is influenced by the shear in a very asymmetric manner, depending on the sign of Sr. Indeed, while the rotation is almost identical to its counterpart in an unbounded shear flow when Sr is negative, it is significantly larger when Sr is positive, even for Reynolds numbers of $O(100)$. These findings are summarized in the fit (40), which predicts the rotation rate well irrespective of the sign of Sr and throughout the range of Reynolds number explored in this investigation. Finally, present results show that the spin-induced contribution to the near-wall lift in the torque-free configuration is directly proportional to the rotation rate. Remarkably, the corresponding prefactor (≈ 0.55) only weakly varies with the Reynolds number and is similar to that previously determined in an unbounded shear flow [11]. These findings allow the fits predicting the lift force on a nonrotating sphere to be extended easily to a torque-free sphere in the form (41) for moderate Reynolds numbers and (42) for $\mathrm{Re} \geqslant 100$.

ACKNOWLEDGMENTS

This work was supported by the Chinese Scholarship Council (CSC). We thank Annaïg Pedrono for her intensive help and support with the JADIM code and the grid generator.

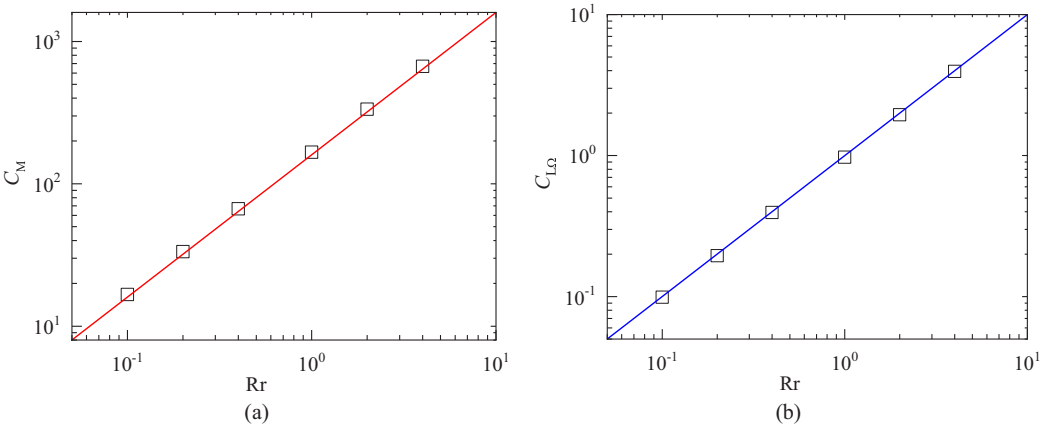

FIG. 27. Loads on a sphere rotating and translating at Reynolds number $\mathrm{Re} = 0.1$ in a fluid at rest. (a) Torque coefficient; (b) spin-induced lift coefficient. □: numerical results. Red and blue lines correspond to the low-Re solutions $C_M = 16\mathrm{Rr}/\mathrm{Re}$ and $C_{L\Omega} = \mathrm{Rr}$, respectively.

TABLE I. Torque, drag, and lift coefficients for a rotating sphere translating parallel to a wall in a linear shear flow at Re = 0.1 and 100 with $L_R = 1.5$ and Sr = 0.5. The first four (six) rows for Re = 0.1 (100) describe the evolution of the force and torque coefficients during the iterative process. The last four (two) rows for Re = 0.1 (100) show how these coefficients vary for prescribed rotation rates slightly larger or smaller than that achieving the torque-free condition.

Re	2Rr/Sr	C_M	C_M/C_{M0}	C_D	C_L
0.1	0.000	35.31	1.000	376.7	2.12
	0.883	−4.90	−0.139	377.2	2.27
	0.760	0.71	0.020	377.1	2.26
	0.778	0.12	0.003	377.0	2.26
	0.831	−2.58	−0.073	377.1	2.27
	0.805	−1.34	−0.038	377.1	2.27
	0.751	1.13	0.032	377.0	2.26
	0.725	2.37	0.067	377.0	2.25
100	0.000	0.0291	1.000	1.21	0.118
	0.726	−0.0111	−0.382	1.23	0.240
	0.449	0.0041	0.142	1.23	0.196
	0.551	−0.0014	−0.048	1.23	0.216
	0.516	0.0003	0.010	1.23	0.212
	0.523	−0.0001	−0.003	1.23	0.213
	0.537	−0.0007	−0.025	1.23	0.214
	0.506	0.0010	0.034	1.23	0.211

APPENDIX: VALIDATION OF THE PROCEDURE USED TO APPROACH THE TORQUE-FREE CONDITION

We start by checking the accuracy of the computed torque and Magnus lift force on a sphere rotating in a unbounded uniform stream. We consider a translation Reynolds number Re = 0.1, for which the asymptotic solution of [2] is supposed to apply. According to this prediction, the torque and spin-induced lift coefficients are, up to higher-order corrections, $C_{L\Omega} = \mathrm{Rr}$ and $C_M = 16\mathrm{Re}^{-1}\mathrm{Rr}$, respectively. Figure 27 compares the numerical results for these two coefficients with the asymptotic prediction over two and a half decades of the rotation rate Rr. Throughout this range of Rr, the deviation from these predictions is less than 4% for both coefficients.

To assess the iteration procedure used to approach the torque-free condition, we consider the case of a rigid sphere moving parallel to a wall in a linear shear flow with $L_R = 1.5$ and Sr = 0.5 at two widely different Reynolds numbers, Re = 0.1 and 100. The initial rotation rate Rr_0 is set to zero and the torque computed at iteration n is used to update Rr via the iterative algorithm $\mathrm{Rr}_{n+1} = \mathrm{Rr}_n + C_{Mn}\mathrm{Re}/16$. In the present tests, iterations are pursued until the magnitude of the torque is reduced to less than 1% of its initial value (instead of 5% in the runs discussed in the paper). The results for the torque, drag, and lift coefficients obtained during this iterative process are summarized in Table I (first four and six rows for Re = 0.1 and 100, respectively). It turns out that the torque-free condition is achieved to within 1% at both Reynolds numbers in at most five iterations. Moreover, virtually no variation in the computed drag and lift coefficients takes place when the ratio $|C_M|/C_{M0}$ becomes less than 5%. For instance, decreasing $|C_M|/C_{M0}$ from ∼5% to a vanishingly small value makes the lift coefficient vary by less than 1.5% at Re = 100. To reconfirm this point, we ran additional cases with prescribed rotation rates yielding torque coefficients of the order of $\pm 0.05 C_{M0}$. These additional data (last four and two rows in Table I for Re = 0.1 and Re = 100, respectively) confirm that the computed drag and lift coefficients vary only marginally with Rr in this range, the

variation in C_L staying again below 1.5%. Based on these tests, we considered that the criterion $|C_M/C_{M0}| < 0.05$ properly approximates the torque-free condition in all cases.

[1] F. P. Bretherton, The motion of rigid particles in a shear flow at low Reynolds number, J. Fluid Mech. **14**, 284 (1962).

[2] S. I. Rubinow and J. B. Keller, The transverse force on a spinning sphere moving in a viscous fluid, J. Fluid Mech. **11**, 447 (1961).

[3] P. G. Saffman, The lift on a small sphere in a slow shear flow, J. Fluid Mech. **22**, 385 (1965).

[4] P. G. Saffman, Corrigendum to "The lift on a small sphere in a slow shear flow", J. Fluid Mech. **31**, 624 (1968).

[5] E. S. Asmolov, Dynamics of a spherical particle in a laminar boundary layer, Fluid Dyn. **25**, 886 (1990).

[6] J. B. McLaughlin, Inertial migration of a small sphere in linear shear flows, J. Fluid Mech. **224**, 261 (1991).

[7] P. Cherukat, J. B. McLaughlin, and A. L. Graham, The inertial lift on a rigid sphere translating in a linear shear flow field, Int. J. Multiphase Flow **20**, 339 (1994).

[8] P. Cherukat, J. B. McLaughlin, and D. S. Dandy, A computational study of the inertial lift on a sphere in a linear shear flow field, Int. J. Multiphase Flow **25**, 15 (1999).

[9] R. Kurose and S. Komori, Drag and lift forces on a rotating sphere in a linear shear flow, J. Fluid Mech. **384**, 183 (1999).

[10] P. Bagchi and S. Balachandar, Shear versus vortex-induced lift force on a rigid sphere at moderate Re, J. Fluid Mech. **473**, 379 (2002).

[11] P. Bagchi and S. Balachandar, Effect of free rotation on the motion of a solid sphere in linear shear flow at moderate Re, Phys. Fluids **14**, 2719 (2002).

[12] R. G. Cox and H. Brenner, The lateral migration of solid particles in Poiseuille flow—I Theory, Chem. Eng. Sci. **23**, 147 (1968).

[13] R. Cox and S. Hsu, The lateral migration of solid particles in a laminar flow near a plane, Int. J. Multiphase Flow **3**, 201 (1977).

[14] P. Vasseur and R. G. Cox, The lateral migration of spherical particles sedimenting in a stagnant bounded fluid, J. Fluid Mech. **80**, 561 (1977).

[15] F. Takemura and J. Magnaudet, The transverse force on clean and contaminated bubbles rising near a vertical wall at moderate Reynolds number, J. Fluid Mech. **495**, 235 (2003).

[16] L. Zeng, S. Balachandar, and P. Fischer, Wall-induced forces on a rigid sphere at finite Reynolds number, J. Fluid Mech. **536**, 1 (2005).

[17] L. Zeng, F. Najjar, S. Balachandar, and P. Fischer, Forces on a finite-sized particle located close to a wall in a linear shear flow, Phys. Fluids **21**, 033302 (2009).

[18] E. S. Asmolov, Lift force exerted on a spherical particle in a laminar boundary layer, Fluid Dyn. **24**, 710 (1989).

[19] J. B. McLaughlin, The lift on a small sphere in wall-bounded linear shear flows, J. Fluid Mech. **246**, 249 (1993).

[20] F. Takemura, J. Magnaudet, and P. Dimitrakopoulos, Migration and deformation of bubbles rising in a wall-bounded shear flow at finite Reynolds number, J. Fluid Mech. **634**, 463 (2009).

[21] F. Takemura and J. Magnaudet, Lateral migration of a small spherical buoyant particle in a wall-bounded linear shear flow, Phys. Fluids **21**, 083303 (2009).

[22] J. Magnaudet, S. Takagi, and D. Legendre, Drag, deformation and lateral migration of a buoyant drop moving near a wall, J. Fluid Mech. **476**, 115 (2003).

[23] P. Cherukat and J. B. McLaughlin, The inertial lift on a rigid sphere in a linear shear flow field near a flat wall, J. Fluid Mech. **263**, 1 (1994).

[24] P. Cherukat and J. B. McLaughlin, The inertial lift on a rigid sphere in a linear shear flow field near a flat wall—Corrigendum, J. Fluid Mech. **285**, 407 (1995).

[25] S. Yahiaoui and F. Feuillebois, Lift on a sphere moving near a wall in a parabolic flow, J. Fluid Mech. **662**, 447 (2010).
[26] D. T. Leighton and A. Acrivos, The lift force on a small sphere touching a plane in the presence of a simple shear flow, Z. Angew. Math. Phys. **36**, 174 (1985).
[27] G. P. Krishnan and D. T. Leighton, Inertial lift on a moving sphere in contact with a plane wall in a shear flow, Phys. Fluids **7**, 2538 (1995).
[28] N. Ekanayake, J. D. Berry, A. D. Stickland, D. E. Dunstan, I. L. Muir, S. K. Dower, and D. J. E. Harvie, Lift and drag forces acting on a particle moving with zero slip in a linear shear flow near a wall, J. Fluid Mech. A **904**, 6 (2020).
[29] N. Ekanayake, J. D. Berry, and D. J. E. Harvie, Lift and drag forces acting on a particle moving in the presence of slip and shear near a wall, J. Fluid Mech. A **915**, 103 (2021).
[30] H. Lee and S. Balachandar, Drag and lift forces on a spherical particle moving on a wall in a shear flow at finite Re, J. Fluid Mech. **657**, 89 (2010).
[31] P. Shi, R. Rzehak, D. Lucas, and J. Magnaudet, Hydrodynamic forces on a clean spherical bubble translating in a wall-bounded linear shear flow, Phys. Rev. Fluids **5**, 073601 (2020).
[32] E. S. Asmolov, A. L. Dubov, T. V. Nizkaya, J. Harting, and O. I. Vinogradova, Inertial focusing of finite-size particles in microchannels, J. Fluid Mech. **840**, 613 (2018).
[33] R. Natarajan and A. Acrivos, The instability of the steady flow past spheres and disks, J. Fluid Mech. **254**, 323 (1993).
[34] P. Shi, Hydrodynamic forces on a sphere translating steadily in a wall-bounded linear shear flow, Ph.D. thesis, Technische Universität Dresden, Dresden, Germany, https://nbn-resolving.org/urn:nbn:de:bsz:14-qucosa2-742474 (2020).
[35] D. Legendre and J. Magnaudet, The lift force on a spherical bubble in a viscous linear shear flow, J. Fluid Mech. **368**, 81 (1998).
[36] E. Loth, Lift of a solid spherical particle subject to vorticity and/or spin, AIAA J. **46**, 801 (2008).
[37] P. Shi and R. Rzehak, Lift forces on solid spherical particles in unbounded flows, Chem. Eng. Sci. **208**, 115145 (2019).
[38] A. J. Goldman, R. G. Cox, and H. Brenner, Slow viscous motion of a sphere parallel to a plane wall—I. Motion through a quiescent fluid, Chem. Eng. Sci. **22**, 637 (1967a).
[39] A. J. Goldman, R. G. Cox, and H. Brenner, Slow viscous motion of a sphere parallel to a plane wall—II. Couette flow, Chem. Eng. Sci. **22**, 653 (1967b).
[40] In (15), prefactors expressed in fractional form were derived analytically by Lovalenti in an Appendix to [23], while those expressed in decimal form originate from the fitted value of the force computed in the form of a volume integral in the same reference.
[41] D. Fabre, J. Tchoufag, and J. Magnaudet, The steady oblique path of buoyancy-driven disks and spheres, J. Fluid Mech. **707**, 24 (2012).
[42] H. Homann, J. Bec, and R. Grauer, Effect of turbulent fluctuations on the drag and lift forces on a towed sphere and its boundary layer, J. Fluid Mech. **721**, 155 (2013).
[43] J. Happel and H. Brenner, *Low Reynolds Number Hydrodynamics* (Prentice-Hall, New York, 1965).
[44] J. Magnaudet, M. Rivero, and J. Fabre, Accelerated flows past a rigid sphere or a spherical bubble. Part 1. Steady straining flow, J. Fluid Mech. **284**, 97 (1995).
[45] D. Legendre, J. Magnaudet, and G. Mougin, Hydrodynamic interactions between two spherical bubbles rising side by side in a viscous liquid, J. Fluid Mech. **497**, 133 (2003).
[46] V. Citro, J. Tchoufag, D. Fabre, F. Giannetti, and P. Luchini, Linear stability and weakly nonlinear analysis of the flow past rotating spheres, J. Fluid Mech. **807**, 62 (2016).
[47] D. Legendre and J. Magnaudet, A note on the lift force on a spherical bubble or drop in a low-Reynolds-number shear flow, Phys. Fluids **9**, 3572 (1997).
[48] F. Takemura, S. Takagi, J. Magnaudet, and Y. Matsumoto, Drag and lift forces on a bubble rising near a vertical wall in a viscous liquid, J. Fluid Mech. **461**, 277 (2002).
[49] M. E. O'Neill, A slow motion of viscous liquid caused by a slowly moving solid sphere, Mathematika **11**, 67 (1964).